Predictions of LAGOON Nose Landing Gear Flow and Noise using Wall-Modeled Large-Eddy Simulations

Man Long Wong*, Gaetan K. Kenway†, Aditya S. Ghate‡, Gerrit-Daniel Stich§, and Cetin C. Kiris¶
NASA Ames Research Center, Moffett Field, CA 94035

Wall-modeled large-eddy simulations (WMLESs) of the LAGOON nose landing gear are conducted with compressible Navier–Stokes equations and immersed boundary technique using the Launch, Ascent, and Vehicle Aerodynamics (LAVA) framework. The simulations are conducted using six different Cartesian octree meshes for the grid sensitivity analysis of the near-field and far-field numerical predictions, where the far-field noise results are computed with the Ffowcs Williams–Hawkings acoustic analogy. The effects of numerical tripping induced at the exact locations of the tripping devices in the experiments are also examined. In general, better comparison with the experimental results are shown for the the near-field results obtained with the simulations under the effects of numerical tripping. The effects of tripping are not significant on the far-field noise calculations and the results have reasonable comparison with the experimental data in the low and medium frequency ranges when an impermeable formulation of the acoustic analogy is used.

I. Introduction

Aircraft noise has adverse effects to the quality of life and health of residents near major airports [1]. As the civil air transportation grows, more aggressive noise reduction goal levels are targeted by governments and organizations. For instance, the NASA Advanced Air Transport Technology (AATT) set a noise goal of 42-52 Effective Perceived Noise Level in decibels (EPNL dB) cumulative below the current levels for the far term period of 2035 [2]. Additionally, the Advisory Council for Aviation Research and Innovation in Europe (ACARE) and the Flightpath 2050 project [3] target a 65% reduction of the perceived noise by 2050, with respect to the noise levels in 2000. As a result, design of more quiet aircrafts is critical to meet increasingly stringent noise regulations. The aircraft noise is mainly composed of two categories: airframe and propulsion noise. While the turbofan engine noise has been greatly reduced over the decades through high bypass ratio, airframe noise becomes a priority concern [4], especially during landing when the propulsion noise is less prominent due to lower engine power settings. The landing gear is one of the dominant airframe noise sources during aircraft takeoff and landing. The noise generated from landing gear is tonal which is caused by resonances from different components, such as pins connecting gear struts [5] and leg-door/hinge-door leading edges [6]. The landing gear noise is also broadband due to the turbulent flow separation and interaction between the turbulent flows and gear components [7]. The tonal and broadband characteristics of the landing gear noise pose challenges on the use of computational fluid dynamics (CFD) and computational aeroacoustics (CAA) tools for accurate predictions of the noise levels during the design of airplanes.

The LAnding-Gear nOise database for CAA validatiON (LAGOON) test case was introduced in the Benchmark for Airframe Noise Computations (BANC) workshops as a benchmark problem on a simplified two-wheel nose landing gear geometry for the validation and verification of different CFD and CAA methodologies [8, 9]. In those workshops, solutions computed by various groups using different gridding strategies and turbulence modeling approaches were compared [10–17]. Three different meshing strategies were mainly employed in the BANC-III workshop, which are respectively multi-block structured, unstructured, and Cartesian octree meshes. Among these three meshing methodologies, the use of Cartesian octree meshing with the immersed boundary method is the most attractive approach since it can save a large amount of labor cost in the preparation of the mesh for a realistic landing gear with hydraulic lines, fasteners, hinges, etc., which is challenging for body-fitted meshing. However, only results from the lattice–Boltzmann methods (LBMs) were shown with that type of meshing using immersed boundary methods. The majority of the

*Science and Technology Corporation, AIAA Member, manlong.wong@nasa.gov.
†Science and Technology Corporation, AIAA Member, gaetan.k.kenway@nasa.gov.
‡Science and Technology Corporation, AIAA Member, aditya.s.ghate@nasa.gov.
§Science and Technology Corporation, AIAA Member, gerrit-daniel.stich@nasa.gov.
¶Computational Aerosciences Branch, AIAA Senior Member, cetin.c.kiris@nasa.gov.

contributions in the BANC-III workshop used the hybrid Reynolds Averaged Navier–Stokes (RANS)/large-eddy simulation (LES) turbulence modeling approach except two groups [13, 18] that applied wall-stress models in LES, which is referred to as wall-modeled LES (WMLES) approach in this work, for the LAGOON problem. In both WMLES and hybrid RANS/LES, only the eddies in the outer portion of the boundary layer are resolved while the energetic eddies in the inner boundary layer are modeled with RANS models. However, in the former approach LES solutions are computed all the way to the walls and the velocity and temperature gradients at the rigid solid boundaries are modeled with shear stress and heat flux boundary conditions [19]. This is different than the hybrid RANS/LES approach where RANS model is used for the inner layer of the boundary layer and LES only exists for the outer layer. WMLES is computationally more affordable compared to wall-resolved LES (WRLES) where eddies in the boundary layer are resolved with much larger amount of grid cells near walls. Aeroacoustic predictions using WMLESs have also been demonstrated for NACA 0012 airfoil [20] and 30P30N three-element airfoil [21].

In this work, Navier–Stokes WMLESs with an equilibrium wall model are conducted for the LAGOON landing gear configuration with Cartesian octree grids using the Launch, Ascent, and Vehicle Aerodynamics (LAVA) framework [22]. The WMLES capabilities of the LAVA framework have already been demonstrated in previous studies [23–27] on various aerodynamics and aeroacoustics problems with curvilinear grids. The WMLES turbulence approach is combined with a recently developed immersed boundary method in this work for the computations of near-field aerodynamics and aeroacoustics, as well as far-field aeroacoustics of the landing gear on Cartesian octree grids. The near-field data is obtained directly from CFD calculations while the far-field noise is computed with the solid (impermeable) formulation of the Ffowcs Williams–Hawkings acoustic analogy [28]. The immersed boundary approach LES has been attempted previously for the Navier–Stokes simulations of a partially-dressed, cavity-closed nose landing gear [29]. While this earlier work was primarily focused on the evaluation of the feasibility of LBM for landing gear aeroacoustics, some preliminary Navier–Stokes simulations without wall modeling and using dissipative numerical discretizations (implicit LES) were also attempted. This current work underscores the need of low dissipation Navier–Stokes formulations with wall modeling and robust immersed boundary treatment for WMLES at higher and more realistic Reynolds numbers. The main objective of this work is the assessment of the WMLES with the new immersed boundary treatment using low dissipation discretizations within the LAVA framework for the study of near-field steady and unsteady flow around the landing gear, as well as the noise radiated to the far-field. The effects and the necessity of the numerical tripping of the boundary layers in this benchmark problem are also analyzed in detail.

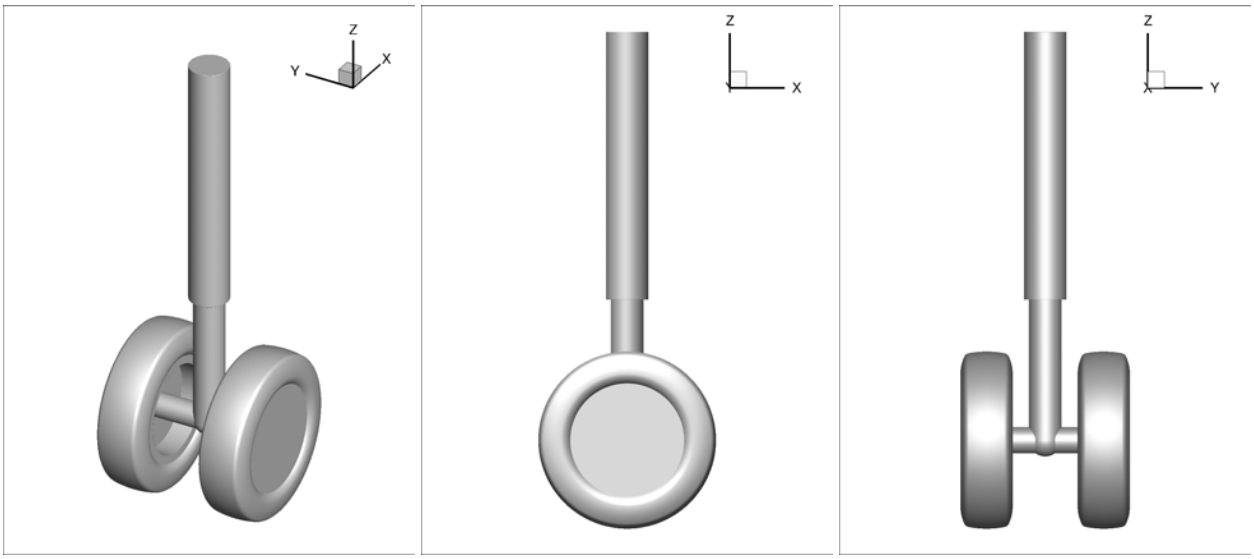
II. Description of Problem

The problem considered is a flow past a simplified nose landing gear. The landing gear is a 1:2.5 scaled version of the Airbus A320 aircraft nose landing gear [30]. The geometry consists of two wheels, the axle, and the main strut composed of the lower and upper legs. The landing gear model is shown in Fig. 1. The wheel diameter D is 0.3 m. The diameters of the axle, lower, and upper legs are 46 mm, 55 mm, and 71 mm respectively. The mid-planes of both wheels are 198 mm apart. Tripping devices were installed on the model in the experiments to promote the transition to turbulent boundary layers. ZIG-ZAP strips were equipped on the frontal parts of the wheels and the axle and main strut were mounted with the CAD-CUT strips aligned at $\pm 60^\circ$ with respect to the mean flow. The location of the transition tripping devices are shown in Fig. 2.

The model was tested in the F2 closed-section wind tunnel and the CEPRA19 (C19) aeroacoustic open-jet facility. Steady and unsteady data of pressure and velocity was provided by the F2 wind tunnel. Pressure measurements were also performed in C19 in addition to the far-field microphone data. Although the freestream Mach numbers are the same, the two facilities have slightly different upstream infinite (freestream) conditions which are tabulated in Table 1. In this work, the freestream conditions of the F2 wind tunnel are chosen for the simulations. The wheel Reynolds number Re_D is around 1.55×10^6 with these freestream conditions.

Facility	p_∞ (Pa)	T_∞ (K)	ρ_∞ (kg m^{-3})	Ma_∞
F2	99447.7	293.56	1.18	0.23
C19	96772.3	288.39	1.18	0.23

Table 1 The upstream flow conditions of the F2 and C19 facilities. p_∞, T_∞, ρ_∞, and Ma_∞ are the freestream pressure, temperature, density, and Mach number respectively.



(a) Isometric view (b) x-z plane (c) y-z plane

Fig. 1 Schematics of the LAGOON landing gear at different views.



Fig. 2 Location of tripping devices colored in red on the LAGOON landing gear.

III. Numerical Approaches and Simulation Setup

A. Numerical Discretization

The compressible Navier–Stokes equations with a subgrid-scale (SGS) model are solved in the LESs. The derivatives of convective fluxes in different directions are computed using the fourth order accurate midpoint-and-node central finite difference scheme [31]. For instance, the derivative of the convective flux vector $\mathbf{F}$ in the x direction is approximated with flux vectors at midpoints $\tilde{\mathbf{F}}_{i+1/2,j,k}$ and nodes $\mathbf{F}_{i,j,k}$:

$$\left.\frac{\partial \mathbf{F}}{\partial x}\right|_{i,j,k} \approx \frac{1}{\Delta x}\left[\frac{4}{3}\left(\tilde{\mathbf{F}}_{i+\frac{1}{2},j,k} - \tilde{\mathbf{F}}_{i-\frac{1}{2},j,k}\right) - \frac{1}{6}\left(\mathbf{F}_{i+1,j,k} - \mathbf{F}_{i-1,j,k}\right)\right], \tag{1}$$

where i, j, and k are the indices in the x, y, and z directions respectively. The convective flux vectors at midpoints, $\tilde{\mathbf{F}}_{i+1/2,j,k}$, are computed with the left- and right-biased interpolated primitive variable vectors using the non-dissipative fourth order central interpolation nonlinearly blended with the third order upwind-biased interpolations. For example, the blending of the left- and upwind-biased interpolation with the central interpolation for a scalar variable at a midpoint,

$\tilde{u}^L_{i+1/2,j,k}$, is carried out as:

$$\tilde{u}^L_{i+\frac{1}{2},j,k} = \xi_{i+\frac{1}{2},j,k}\tilde{u}^{L,upwind}_{i+\frac{1}{2},j,k} + \left(1 - \xi_{i+\frac{1}{2},j,k}\right)\tilde{u}^{central}_{i+\frac{1}{2},j,k}, \tag{2}$$

where $\tilde{u}^{L,upwind}_{i+1/2,j,k}$ and $\tilde{u}^{central}_{i+1/2,j,k}$ are values from the left-biased and central interpolations respectively. The blending of the right-biased interpolation with the central interpolation for $\tilde{u}^R_{i+1/2,j,k}$ is performed in the same way. Evaluation of the inviscid flux at midpoints, as opposed to nodes, results in reduced aliasing errors and hence improves nonlinear robustness for turbulent flows. The sensor $\xi_{i+1/2,j,k}$ is close to zero in turbulent regions (except near convex/concave corners of the geometry) and is one otherwise. The concept of nonlinear blending between upwind-biased and central interpolations is similar to [32] but the sensor used in this work is a physics-based sensor that compares the magnitudes between the vorticity and the strain rate to detect turbulent regions. The weighted essentially non-oscillatory (WENO) interpolation with the classical nonlinear weights [33] is used for a limited amount of cells that are close to coarse-fine grid interfaces and at trapped cells near the geometry to increase the robustness of the scheme. As a result, the scheme becomes a weighted compact nonlinear scheme (WCNS) [32, 34–38] in those regions. The flux vectors at the midpoints are computed with the left- and right-biased interpolated variables, $\tilde{u}^L_{i+1/2,j,k}$ and $\tilde{u}^R_{i+1/2,j,k}$, using the Harten–Lax–van Leer contact (HLLC) approximate Riemann solver [39] The wavespeed estimates from [40–42] with the Roe averaging are used in the HLLC Riemann solver. The viscous and diffusive flux vectors are evaluated at the midpoints using second order accurate staggered finite differencing, followed by a second order accurate scheme for the derivatives. The explicit third order total variation diminishing Runge–Kutta (RK-TVD) [43] time stepping scheme is employed.

B. Wall-Model and Immersed Boundary Method for Large-Eddy Simulation

In the wall-stress WMLES approach, the LES solutions are computed all the way to the walls with wall stress and heat flux boundary conditions provided by the wall models (WMs), whereas the wall models use the LES solutions close to the wall as outer boundary conditions. The WMLES method considered in this work is a physics-based approach which can be simply categorized into the algebraic, ordinary differential equation (ODE) based, and partial differential equation (PDE) based models. The most general method is the PDE-based one where the thin boundary layer (TBL) PDE are solved with most or all of the terms in the left hand side of the equations retained. However, a near wall separate RANS grid is required in this method for solving the TBL PDE, apart from the LES grid. A computationally more affordable method is the ODE-based equilibrium WMLES where the exact balance of the left hand side terms in the TBL PDE are assumed, thus only ODE are solved. In this work, the less expensive algebraic equilibrium WMLES is used where approximate solutions to the ODE-based equilibrium WMLES are sought through algebraic equations with a nonlinear solver. A schematic diagram showing the working principles of various WMLES methods is given in Fig. 3. More details on the wall-stress WMLES can be found in previous literature review articles [19, 44–46]. The algebraic wall model implemented in this work is an analytical law with smooth blending between the viscous sublayer and log-layer. Wall-model inputs are obtained via sampling at a distance of around one Δx away from the wall, where Δx is the grid spacing. All simulations use the Vreman SGS model [47] with a fixed model constant taken to be $c_{\text{sgs}} = 0.08$.

A ghost cell immersed boundary method (IBM) [48] is used for the numerical discretization of convective fluxes near walls to impose the no-penetration boundary conditions. The ghost cell IBM is a sharp IBM approach where cells inside the body are filled with appropriate flow data with the aid of surface meshes, which are surface triangulations of the solid geometry, to enforce the boundary conditions. A detailed discussion of the current immersed boundary WMLES formulation is beyond the scope of the present work and will be addressed in a future manuscript. The methodology has been validated using a sequence of wall-bounded flows including: a) zero-pressure gradient grid aligned and misaligned flat plates, b) NASA wall-mounted hump [49, 50], c) NACA 23012 airfoil with leading edge icing [51], d) high lift common research model [52], e) partially-dressed, cavity-closed nose landing gear [53].

C. Simulation Configurations and Tripping Strategies

Six different Cartesian octree grids with local mesh refinement only around the landing gear and the wake region are designed to facilitate grid sensitivity analysis. The landing gear is placed in the center of a cubic computational domain with a cube length of 157.2864 m ($\approx 524D$) for all of the grids, except grid F with a cube length of 209.7152 m ($\approx 699D$). For each grid, there is at least ten levels of mesh refinement of isotropic Cartesian cells with a refinement ratio of two in each direction between successive grid levels. The grids are labeled as grids A, B, C, D, E, and F in the ascending order of the finest grid level resolution. The grids A, B, C, and D have the same grid refinement conditions.

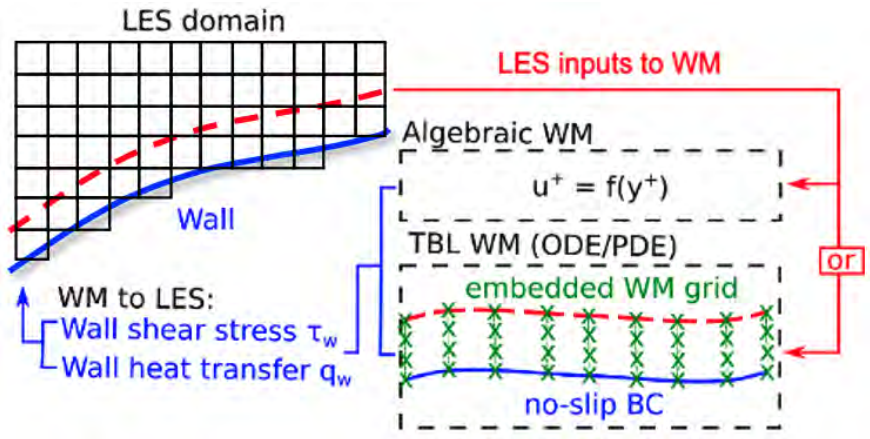


Fig. 3 Schematic showing the working principles of different WMLES methods.

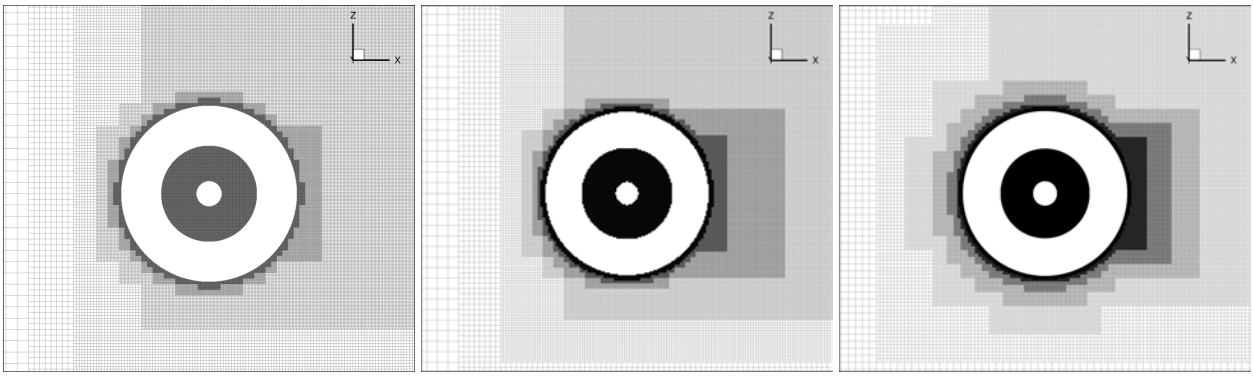
For these four grids, the finest level of grid cells is deployed on the surfaces of the wheels, the axle, and the main strut, with a thickness of around 8 grid cells. Two boxes of refinement in the wake region around the back of the two wheels are used to refine the grid up to the second finest level. There are two additional larger refinement boxes with successively coarser grid levels to gradually coarsen the grid downstream of the wake of the landing gear. Grids E and F also have the finest level of grid cells covering the surfaces of the landing gear, but with thicknesses of 16 and 24 grid cells respectively. Besides, there are more levels involved in the cascade of boxes for the gradual coarsening of the wake grid, with four and five levels of boxes respectively for grids E and F. The number of cells for the three finest grids, grid D, E, and F, per wheel diameter are 500, 1000, and 1500 respectively. If the smaller axle diameter is considered as the characteristic length, there are around 230 cells per axle diameter for grid F. The details of the two grids, the time step sizes, and the performance of the simulations are tabulated in Table 2. The simulations were conducted with the Intel Skylake processors (20-core Xeon Gold 6148 model). Note that the spacings of the surface elements (triangles) are chosen to be at least as small as the corresponding volume grid cell spacings. Figs. 4 and 5 show the local mesh refinement and the grid hierarchy through the cutting planes of grid D, grid E, and grid F respectively.

Grid	Number of mesh levels	Minimum grid cell spacing (mm)	Number of grid cells (million)	Surface element spacing (mm)	Number of surface elements (million)	Time step size (μs)	CPU hours per 1 ms of physical time
A	11	4.8	2.197	~ 0.50	5.763	~ 5.79	1.322
B	12	2.4	6.130	~ 0.50	5.763	~ 2.82	2.385
C	13	1.2	22.16	~ 0.50	5.763	~ 1.37	9.152
D	14	0.6	100.5	~ 0.50	5.763	~ 0.70	55.32
E	15	0.3	309.0	~ 0.30	15.94	~ 0.35	303.0
F	16	0.2	737.9	~ 0.15	63.76	~ 0.23	920.5

Table 2 The details of different grids used for grid sensitivity study and the performance of simulations with the grids.

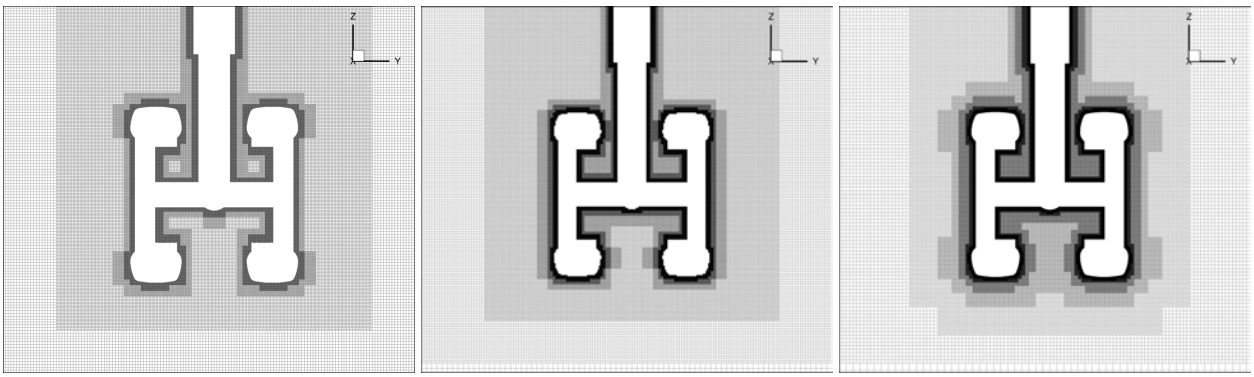
All simulations are initialized with freestream conditions. The flow is in the positive x direction while y and z are the transverse and vertical directions. Because of the impulsive start of the simulations, a Courant–Friedrichs–Lewy (CFL) number of 1.0 is used for better numerical robustness during the first 5 convective time units (CTUs), where the CTU is based on the wheel diameter and the freestream velocity magnitude. After that, the CFL number is raised to 1.5 for the remaining course of each simulation. We have also verified that the results computed with CFL numbers of 1.0 and 1.5 are generally the same. Note that the performance presented in the last column of Table 2 is based on CFL number of 1.5. The data sampling starts at around 100 CTUs, which corresponds to 0.38 s, when the initial transients are flushed out. The sampling continues for another 200 CTUs ($\approx$ 0.76 s). Extrapolation far-field boundary conditions are applied on all domain boundaries. The domain boundaries are far enough from the landing gear with very coarse grid resolution and upwind-biased scheme such that there is sufficient numerical dissipation to eliminate any unphysical reflected waves.

As mentioned previously, tripping devices were installed on the landing gear model to trigger laminar-turbulent



(a) Grid D (b) Grid E (c) Grid F

Fig. 4 Cross-sections of different grids at wheel mid-plane (y = 99 mm) showing the grid hierarchies.



(a) Grid D (b) Grid E (c) Grid F

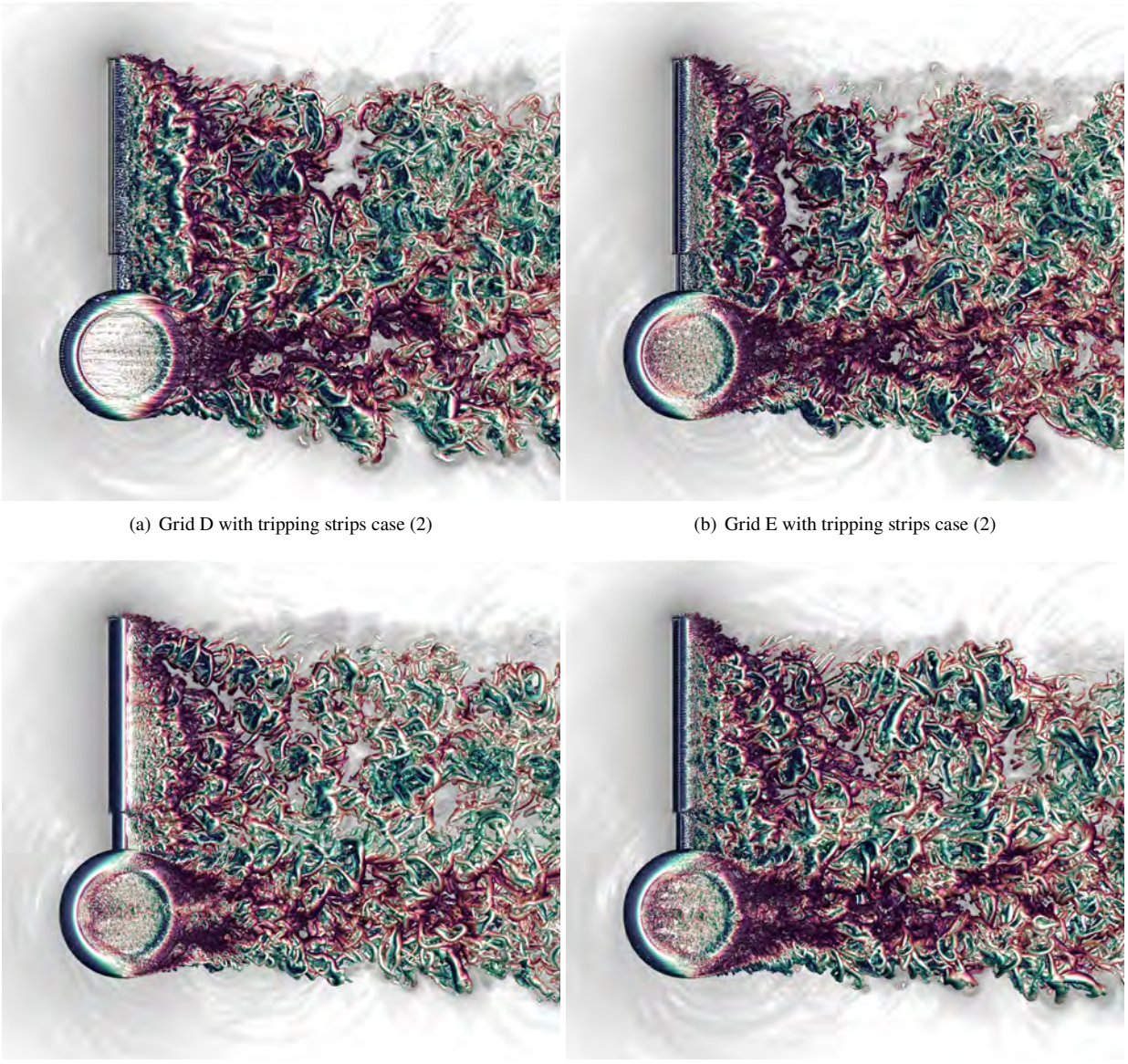
Fig. 5 Cross-sections of different grids at $x = 0$ showing the grid hierarchies.

transition. The characteristic length scales of these devices, such as the thickness of tripping dots on the axle and main strut, and the roughness lengths of the strips on the wheels, are too small to be well resolved by the simulations. In order to mimic the laminar-turbulent transition effects triggered by tripping devices in the experiments, numerical tripping strips or lines are placed at the actual locations of the tripping strips in the experiments. These numerical tripping strips are small dashed circular tubes that represent source terms in the compressible Navier–Stokes equation with user-tuned characteristic length and time scales to perturb the flow for transition. All these numerical tripping lines have a diameter of $4\Delta x$ and a time scale of $6\Delta t$. These dashed lines also have dash length and interval spacing of 3.6 mm. In other words, there are more grid cells per dash and interval spacing between dashes when the grid is refined. This is found to be useful for more consistent results between grids of different resolutions. Two tripping cases are considered in this work: (1) with numerical tripping strips only placed at the axle and the main strut, and (2) with numerical tripping strips placed at all tripping locations in the experiments.

IV. Flow Visualizations

Figs. 6 and 7 display the iso-surfaces of Q-criterion at value of 1.0×10^6 s^{-2} at around 300th CTU. These Q-criterion iso-surfaces show locations where the vorticity magnitude is much larger than the strain rate magnitude. Strong flow unsteadiness and the large amount of small turbulent eddies shed from the landing gear can be seen from the iso-surfaces of Q-criterion. The density gradient magnitude contours on the two-dimensional (2D) planes at $y = 0$ and $z = 0$ display the acoustic waves generated by the unsteady turbulent flow. From Fig. 6, it is observed that smaller vortices are generated downstream of the vertical tripping lines on the strut when the grid is refined from grids D to F. There are also more vortices created on the outer side of the wheel. Comparing the simulations with and without the tripping strips on grid F, it is obvious that the numerical tripping lines along the main strut are effective in generating more vortices. In

Fig. 6, it is shown that the boundary layer flows on the upper surfaces of the wheels transition to turbulence at more upstream locations when the grid is refined from grid resolutions D to F. The tripping lines on the wheels only have minor effects on the transition of the boundary layers, by comparing the cases with and without tripping strips for grid F. While not shown, the effects of tripping strips on the boundary layer transitions are also small for other grid resolutions.



(a) Grid D with tripping strips case (2)

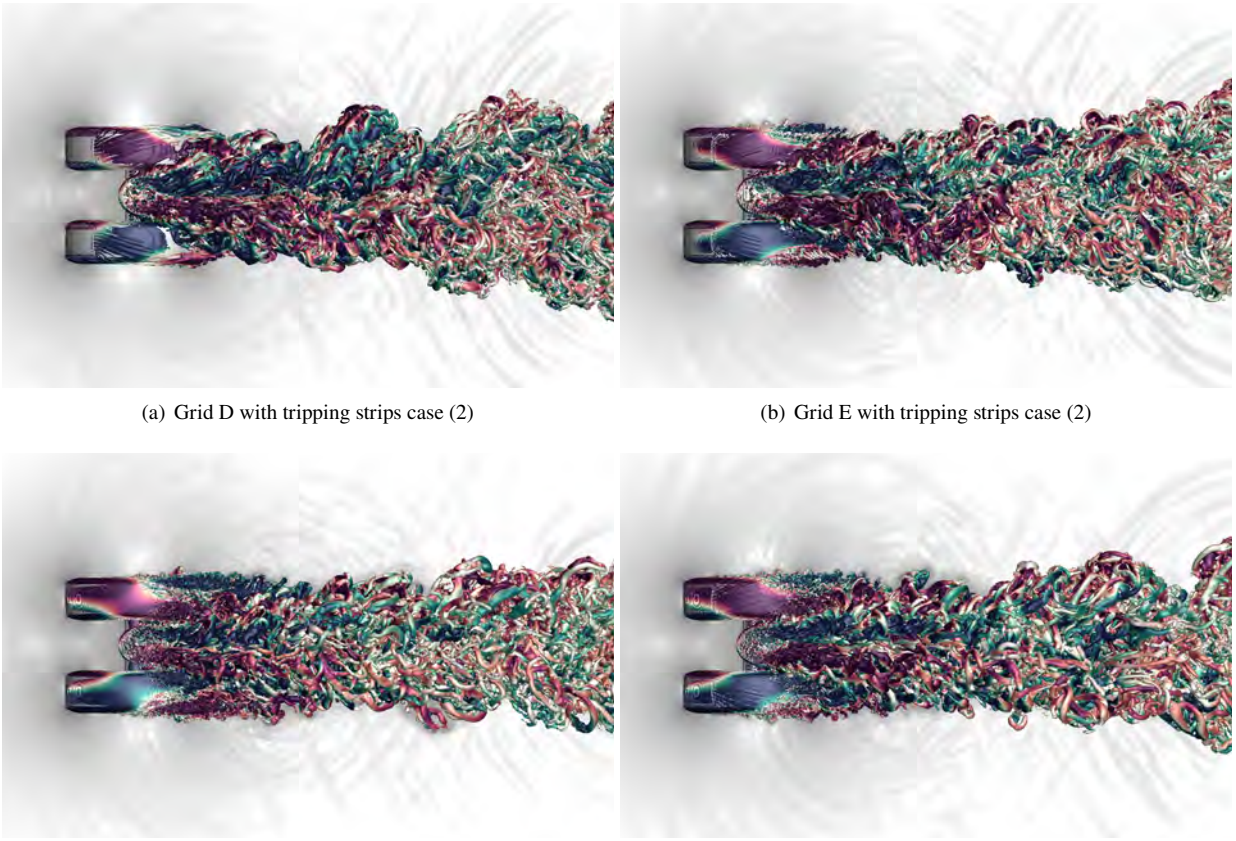
(b) Grid E with tripping strips case (2)

(c) Grid F without tripping strips

(d) Grid F with tripping strips case (2)

Fig. 6 Iso-surfaces of Q-criterion at the value of 1.0×10^6 s^{-2} **on top of density gradient magnitude iso-contours from** 5.0×10^{-3} kg m^{-4} **to** 5.0×10^3 kg m^{-4} **in the** $y = 0$ **plane at** $\sim$ 300th **CTU. The iso-surfaces are colored by** y**-component of instantaneous velocity in the range of** ± 18 m s^{-1}**.**

The surface mean pressure coefficient distributions computed with different grids are viewed from upstream in Fig. 8. The mean pressure coefficient is computed as $c_p = (\bar{p} - p_\infty)/(\rho_\infty U_\infty^2/2)$, where $\bar{p}$, p_∞, ρ_∞, and U_∞ are the mean pressure, freestream pressure, freestream density, and freestream velocity magnitude respectively. Comparing the cases without the tripping strips, there are only minor differences in the results between grids B to F, except for grid A, which is due to poor grid resolution. The effects of the tripping can be seen in the results obtained with tripping strips, which appear as dashed lines in the contours of pressure coefficient. No noticeable grid sensitivities of pressure



(a) Grid D with tripping strips case (2)

(b) Grid E with tripping strips case (2)

(c) Grid F without tripping strips

(d) Grid F with tripping strips case (2)

Fig. 7 Iso-surfaces of Q-criterion at the value of 1.0×10^6 s^{-2} on top of density gradient magnitude iso-contours from 5.0×10^{-3} kg m^{-4} to 5.0×10^3 kg m^{-4} in the $z = 0$ plane at $\sim$ 300th CTU. The iso-surfaces are colored by y-component of instantaneous velocity in the range of ± 18 m s^{-1}.

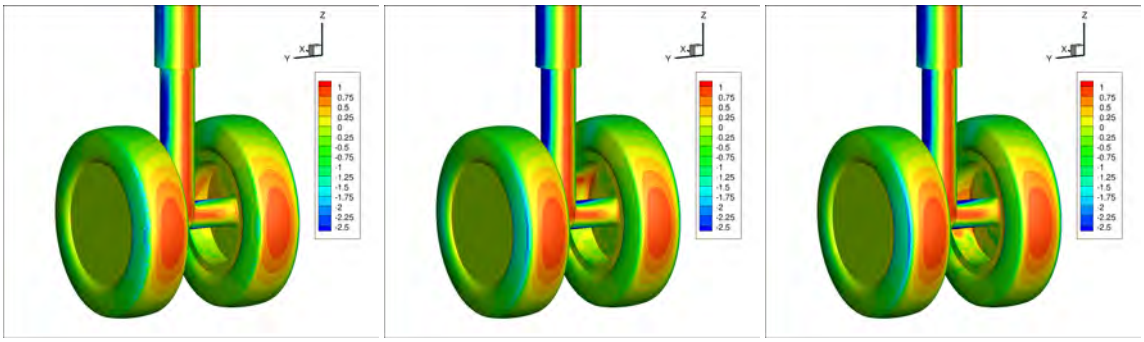
coefficient distributions are found between grid D, grid E, and grid F for these cases with tripping but there are large differences in the contours between cases with and without tripping strips, particularly on the sides of the main strut. It is also noticed that the tripping lines on the wheels have small effects on the pressure coefficient contours except in the regions close to those tripping lines, by comparing the results between the two tripping cases.

V. Near-field Results Without Effects of Tripping Strips

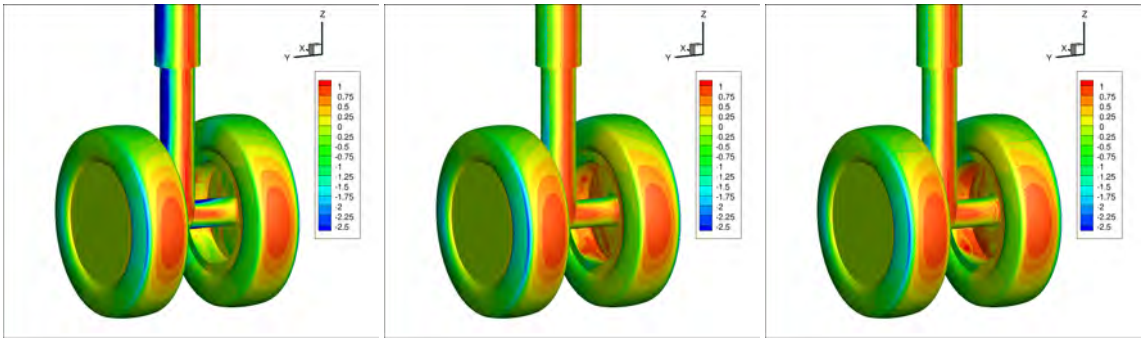
The simulation results without the use of any tripping strips are compared with the experimental data in this section. Pressure measurements were made in the F2 and C19 facilities with static pressure taps, unsteady pressure transducers (Kulites), and microphones. Velocity fields were mainly measured through particle image velocimetry (PIV) and laser Doppler velocimetry (LDV) in the F2 wind tunnel.

A. Mean Pressure Coefficients

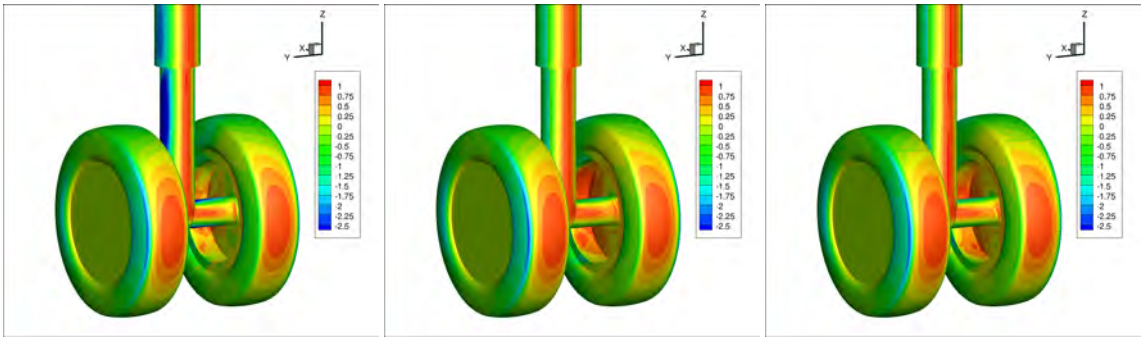
Mean wall pressure is measured by 64 static pressure taps mounted on the landing gear model during the experiments. The locations of the steady pressure sensors are shown in Fig. 9. A complete set of c_p values at the 64 static pressure probe locations is provided by the F2 wind tunnel and the results are averaged from three realizations. In addition, the values at the circular ring around the left wheel were also measured from the C19 open jet aeroacoustic facility [9]. The circular ring around the left wheel consists of 37 pressure sensors in the range of $\pm 120^\circ$ on the wheel periphery. The comparison of the pressure coefficients obtained with the simulations and the experimental results at these 37 locations is shown in Fig. 10(a). Only very small grid sensitivities are observed at most of these locations, except for the



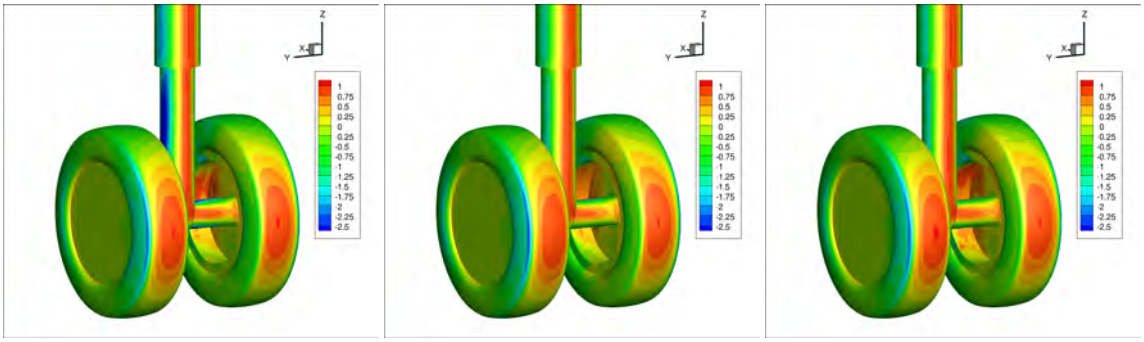
(a) Grid A without tripping strips (b) Grid B without tripping strips (c) Grid C without tripping strips



(d) Grid D without tripping strips (e) Grid D with tripping strips case (1) (f) Grid D with tripping strips case (2)



(g) Grid E without tripping strips (h) Grid E with tripping strips case (1) (i) Grid E with tripping strips case (2)

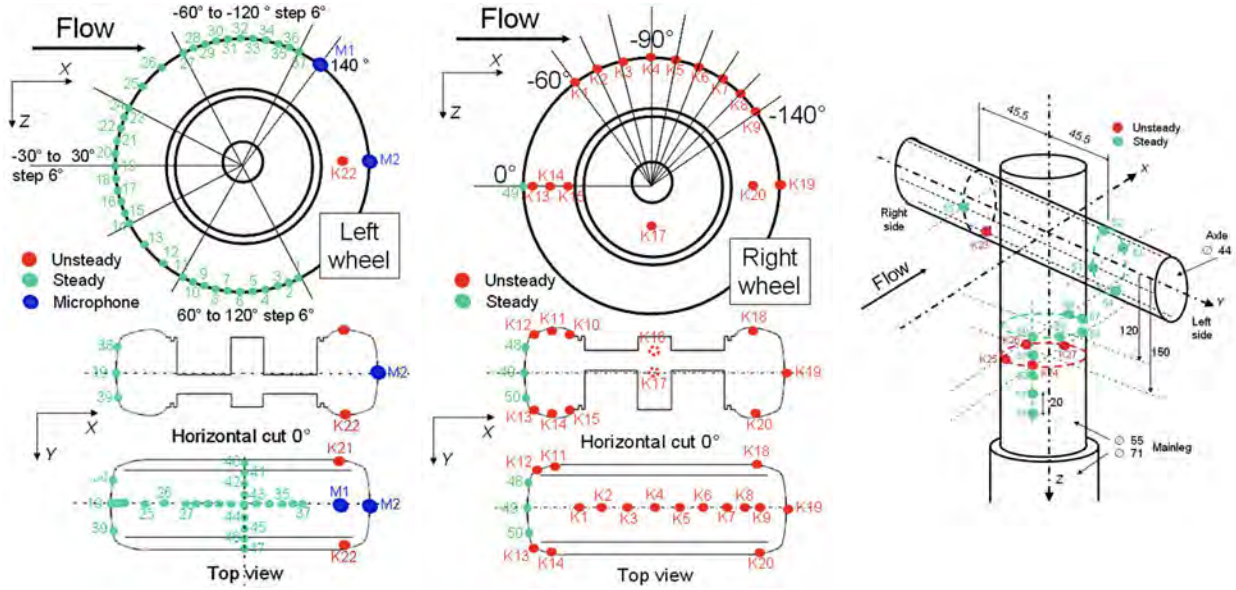


(j) Grid F without tripping strips (k) Grid F with tripping strips case (1) (l) Grid F with tripping strips case (2)

Fig. 8 Mean pressure coefficient distributions on the surface of the landing gear.

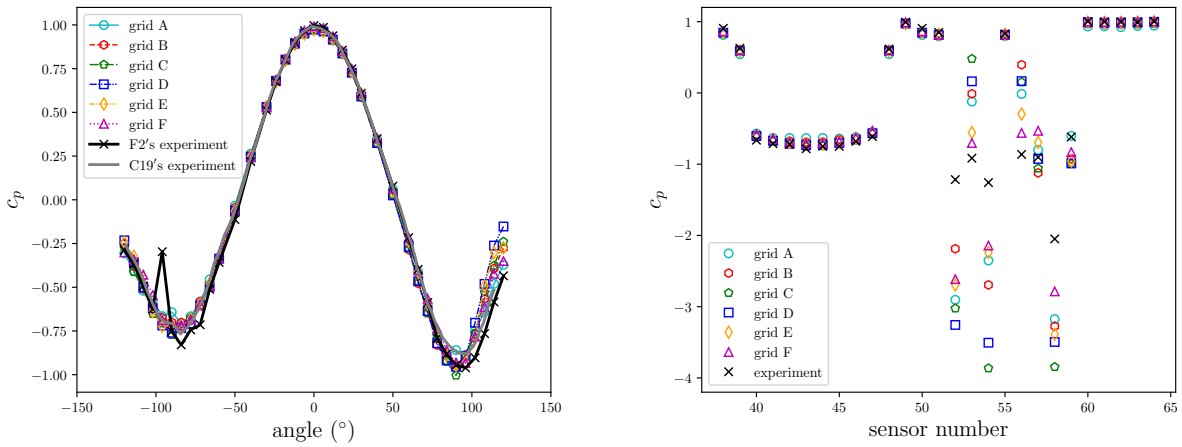
lowest resolution grid A. The largest grid sensitivity is observed in the adverse pressure gradient region at the top of the wheel (positive angles) that is affected by the wake of the main strut. At the bottom of the wheel (negative angles), the simulation results agree better with the experimental results from the C19 open-jet facility in regions around $-90°$ where the experimental results exhibit some discrepancies. The simulations are conducted in an open domain, thus are expected to match the results from C19 facility better than the F2 closed-loop wind tunnel. In the F2 closed-loop wind tunnel, the flow is affected by the solid blockage effect from the side walls. This may explain the discrepancies between the experimental results from the C19 and F2 wind tunnels at around $\pm 90°$. Interesting, the c_p values computed with the simulations match the results from the F2 wind tunnel rather than the C19 facility much better from $70°$ to $90°$ on the top of the wheel.

Fig. 10(b) shows the comparison of the pressure coefficients at other locations. These mainly include a transverse tap located at $-90°$ on the wheel, linear and curricular taps on the lower leg, and linear and circular taps around the axle. The transverse line on the wheel has 9 sensors #40-#47. The simulation results compare reasonably well with the experimental results on this line. The linear tap on the lower leg consists of sensors #60-#64. The simulation results match those from the experiments well at these front stagnation points. The circular taps around the lower leg are formed by sensors #56-#60. The simulation results show large grid sensitivity at this circular ring and large discrepancy between the simulation and experimental results can be seen. Finally, the circular and linear taps on the axle are formed by sensors #51-#54, and sensors #51 and #55 respectively. Except at the linear tap that is formed by the stagnation points, the simulation results at these axle locations are very sensitive to the grid resolution and have large differences compared with the experimental results. Note that the Reynolds numbers based on the axle, lower leg, and upper leg are 2.3×10^5, 2.8×10^5, and 3.7×10^5 respectively. These Reynolds numbers fall into the sub-critical and critical ranges of flow past a cylinder. In these ranges, the wake topology changes drastically with the Reynolds number due to the presence of laminar separation bubbles with combined effects of flow separation, transition to turbulence in the separated regions, and reattachment of the flow [54]. Accurate modeling of the flow physics in the laminar separation bubble and the wake at these Reynolds numbers is known to be a challenging task and this may also explain the large grid sensitivities of c_p at these axle's and strut's sensors.



(a) Left wheel (b) Right wheel (c) Main strut and axle

Fig. 9 Schematic showing the pressure instrumentation locations (part of the LAGOON database, property of Airbus/ONERA [30]). The green dots represent the locations of the static pressure taps; the red dots represent the locations of the unsteady pressure sensors; and the blue dots represents the 2 microphone locations.



(a) Circular ring around the wheel

(b) Other locations

Fig. 10 Mean pressure coefficients on the LAGOON landing gear for simulations without tripping strips. Cyan circles (with solid line): grid A; red hexagons (with dashed line): grid B; green pentagons (with dash-dotted line): grid C; blue squares (with dash-dot-dotted line): grid D; orange diamonds (with dash-triple-dotted line): grid E; magenta triangles (with dotted line): grid F; black crosses (with thick solid line): experimental results of F2 wind tunnel; gray thick solid line: experimental results of C19 facility.

B. Pressure Power Spectral Densities

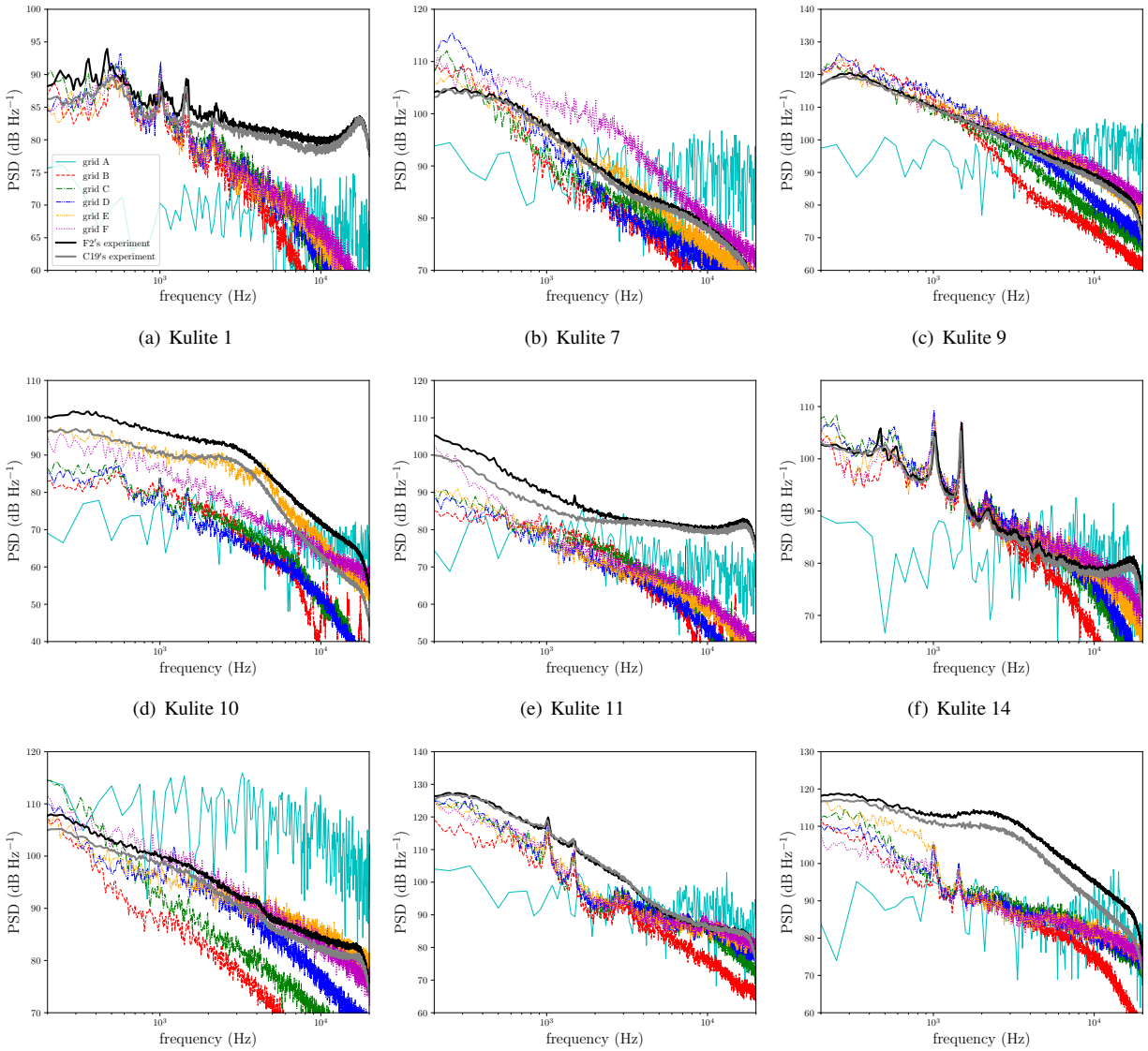
There were 27 Kulite pressure sensors installed on the landing gear for the measurement of the unsteady wall pressure fluctuations in the experiments, as depicted in Fig. 9. The unsteady pressure values were measured in both F2 and C19 wind tunnels. In Fig. 11, the power spectral densities (PSDs) computed with the unsteady pressure data from the simulations are compared with those from the experiments. Following the experimental measurements, all PSDs in this work are computed with a bin frequency of 10 Hz. The Hann window with 75% overlap is chosen for windowing. The reference PSD value of 4.0×10^{-10} Pa^2 Hz^{-1} is used to normalize the pressure PSDs. The sampling intervals are around 5 time steps for grid A, 10 time steps for grids B to E, and 20 time steps for grid F.

Figs. 11(a) to 11(c) show the comparison between the PSDs obtained from the simulations with the two sets of experimental results at three different Kulite locations on the right wheel, from the attached to the flow separated regions. Grid convergence can be observed at the Kulites 1 and 9, while large grid sensitivity can be seen at Kulite 7 even at high grid resolution. The Kulite 7 is near the flow separation point of the boundary layer. The flow separation point predicted by the simulation is sensitive to the grid. When the grid is finer, the flow separation appears to happen at a location that is slightly further upstream and hence there is larger pressure fluctuation. There are smaller cut-off frequencies, or large under-predictions of PSDs from the simulations in the high frequency range at Kulite 1. A physical tripping strip is installed just upstream of Kulite 1 in the experiments and the lack of modeling of the tripping by these simulations is the root of the discrepancies, as will be shown in the next section. Nevertheless, the two tonal peaks at around 1 kHz and 1.5 kHz are captured accurately by the simulations with different grids, except grid A with the lowest grid resolution. At Kulite 9, the flow has become fully turbulent and is characterized by the boardband noise spectrum. The PSD spectra at this Kulite are accurately predicted with the high resolution grids E and F for almost two decades of frequencies.

Figs. 11(d) and 11(e) compare the PSDs at Kulites 10 and 11 located at the front part of the wheel's outer side where Kulite 10 is upstream of the Kulite 11. There is around 5 dB disagreement between the two experimental PSD curves at Kulite 10 across the entire range of frequencies. Large grid sensitivities on the PSDs can also be seen at this Kulite. The PSD computed with grid E agrees almost perfectly with the PSD measured from C19 facility. The spectrum obtained with grid F has reasonable agreement with the C19's PSD, except with discrepancies in the medium frequency range. The curvature of the external side of the wheel is poorly represented by the lower resolution grids, and thus there are large under-predictions in the PSDs. At Kulite 11, all of the simulations under-predict the PSD levels across the entire frequency range. The tripping strips installed on the front part of the wheel may introduce effects at this Kulite

which are not accounted by these simulations. Fig. 11(g) shows the PSDs at Kulite 22 which is located at the rear part of the wheel's outer surface. This Kulite is in a region that is fully turbulent. Both simulations with grids E and F can capture the PSD levels well for around two decades of frequencies. The PSDs of Kulite 14 at the front part of the inner side of the wheel are shown in Fig. 11(f). Except for the simulation with lowest resolution grid A, the two tones at around 1 kHz and 1.5 kHz can be accurately predicted by all simulations. The tones are generated by the resonance in the cavity between the two wheels [15, 55]. Slight over-predictions are noticed in the high frequency range for the PSDs computed with grids E and F.

Finally, the PSDs at Kulites 23 and 26, which are mounted on the axle and lower leg respectively, are compared in Figs. 11(h) and 11(i). None of the simulations can predict the spectra well at these two locations. This is due to the fact that the effects from the tripping dots on the main strut and axle are not modeled in these simulations.



(a) Kulite 1 (b) Kulite 7 (c) Kulite 9

(d) Kulite 10 (e) Kulite 11 (f) Kulite 14

(g) Kulite 22 (h) Kulite 23 (i) Kulite 26

Fig. 11 Pressure PSDs at different locations of LAGOON landing gear for simulations without tripping strips. Cyan solid line: grid A; red dashed line: grid B; green dash-dotted line: grid C; blue dash-dot-dotted line: grid D; orange dash-triple-dotted line: grid E; magenta dotted line: grid F; black thick solid line: experimental results of F2 wind tunnel; gray thick solid line: experimental results of C19 facility.

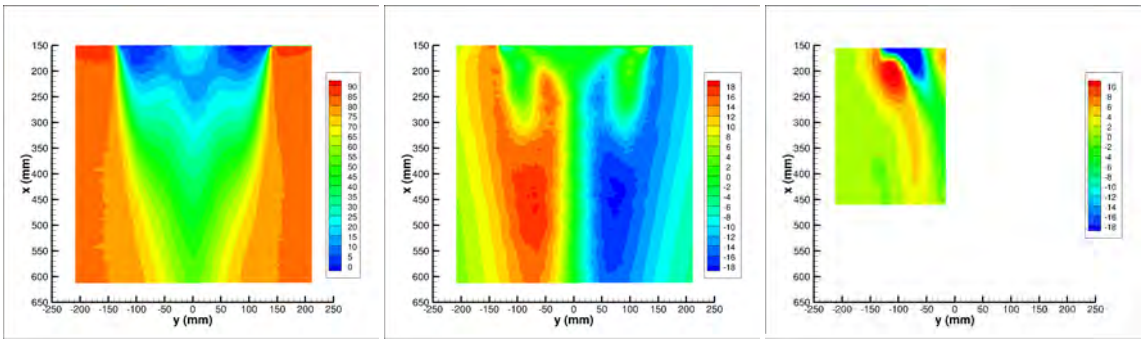
C. Mean Velocity Fields

Fig. 12 compares the mean velocity components obtained from the simulations and the experiments on a 2D x-y plane at $z = 0$. This 2D plane is placed in the wake region downstream of the landing gear. The mean streamwise (x-direction) and transverse (y-direction) velocity components, U and V, were measured with PIV in the F2 wind tunnel. The vertical (z-direction) velocity component W was not addressed by the PIV measurements but was measured using LDV in a limited area. Only the simulation results with the higher resolution grids, grids D, E, and F, are visualized and analyzed in this section. In general, the contours obtained with the simulations are highly symmetric and are in the same symmetry levels as the experimental results, indicating that a sufficient amount of simulation time is performed. Compared with the experimental results, there are over-predictions of U with the simulations in the middle part of the wake near the landing gear although the over-prediction decreases when the grid is refined. As for V, all simulations under-estimate the magnitude of this velocity component and the under-prediction is the worst for simulation on grid F. Although only a limited area of data is provided from the experiments, large variation of W is observed in this small window of the wake. This velocity component is strongly positive and negative in the outer and inner regions respectively. The component is also slightly positive in the core of the wake that is close to the landing gear. Again, large grid sensitivity is shown for W. The region with negative contours is absent for the grids D and E. Only simulation with grid F can reproduce the contours with negative values.

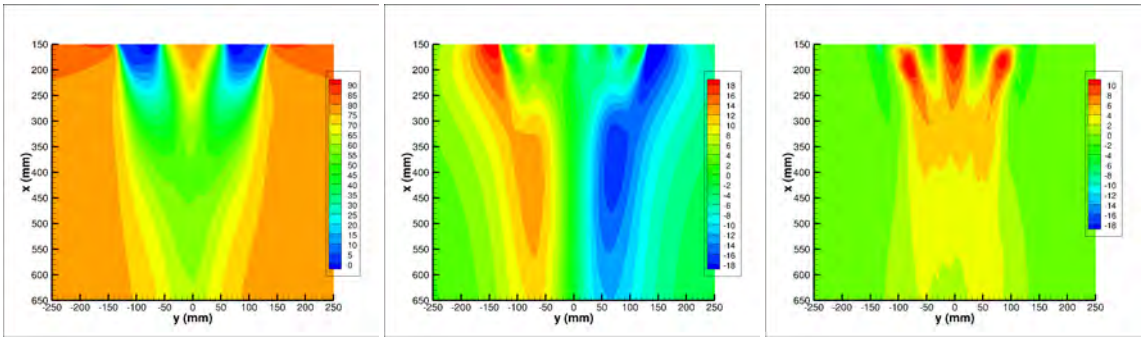
Mean velocity profiles on a number of lines around the landing gear were measured with LDV in the F2 wind tunnel. We have chosen three measurement lines at the periphery of one of the wheels to examine the boundary layer profiles. These three lines, lines 13, 12, and 20 are on the median plane of the wheel and are normal to the bottom surface of the wheel, as indicated in Fig. 13. Lines 13 and 20 are in the regions with favorable and adverse pressure gradients respectively while line 12 is in between the two lines and is aligned with the z axis. The mean streamwise and vertical velocity components, U and W, are shown in Fig. 14. The grid sensitivities of these mean velocity components are small, relative to the freestream velocity magnitude. The profile of U on line 12 are better captured by the simulations relative to those on lines 13 and 20 with under-predictions. The W profiles are also under-estimated on all three lines. The discrepancies of the mean velocity component U between the simulations and experiments may be due to the use of an open domain for the simulations while the experimental data was measured under the blockage effects in the F2 closed-loop wind tunnel. In [55], similar levels of under-estimation are also observed in the profiles of U and W on lines 13 and 20 from the hybrid RANS/LES simulations in an open domain. In a later section, it is also shown that the profiles of W from the simulations are improved with the effects of numerical tripping.

D. Velocity Power Spectral Densities

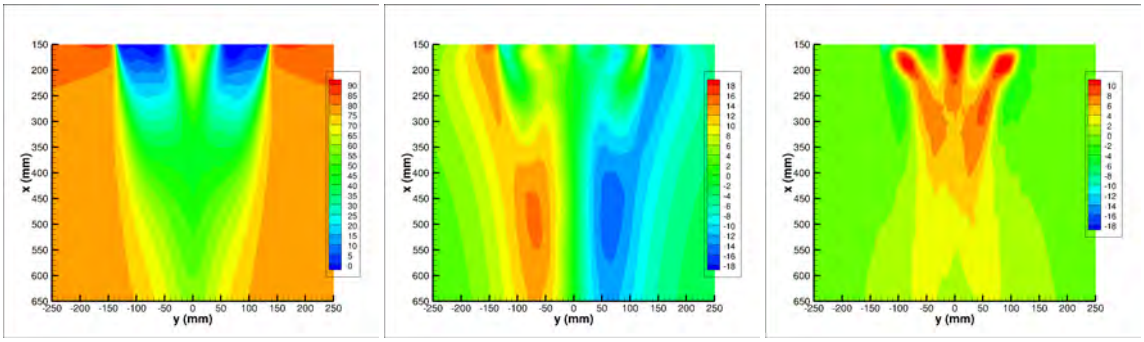
Velocity spectral data was measured at different point probes through LDV. Here, three out of the five LDV point probes from 10 mm to 90 mm downstream of the wheel shown in Fig. 15 are investigated. Only the unsteady data of the streamwise and the vertical components of the velocity, u and w, are measured through LDV in the experiments. As in the computations of the pressure PSDs, the bin frequency of 10 Hz is chosen with the Hann windowing and 75% overlap. Comparisons of velocity PSDs normalized with the reference value of 1 $m^2\ s^{-2}\ Hz^{-1}$ are shown in Fig. 16. Ignoring the results from grid A due to poor resolution, it can be seen in the plots that PSDs of u and w predicted have larger cut-off frequencies with higher grid resolution in general. Note that the cut-off frequencies of grid F are smaller than those of grid E at 90 mm downstream because the wake grid resolution of the former is lower than the latter at that location. For the point probe that is closest to the wheel, the PSD levels in the low frequency range are under-estimated by all of the simulations. When the point probe is being moved away from the wheel, there are improvements in the predictions for the low frequency PSD levels.



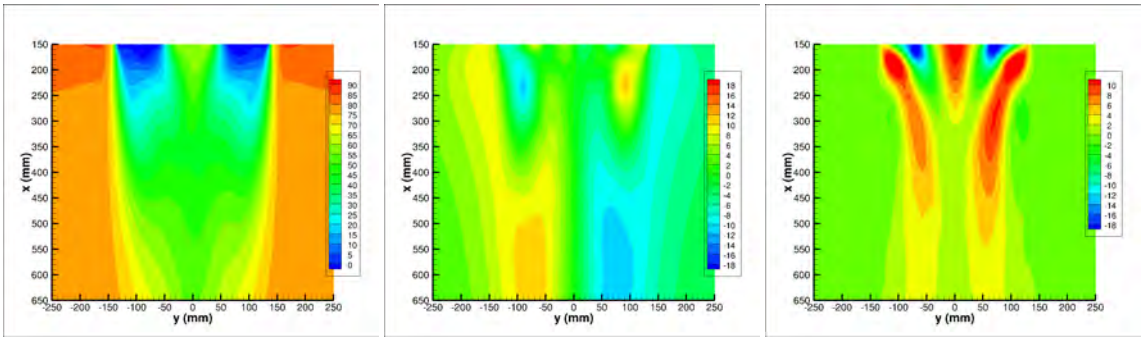
(a) Experiment, U (b) Experiment, V (c) Experiment, W



(d) Grid D, U (e) Grid D, V (f) Grid D, W

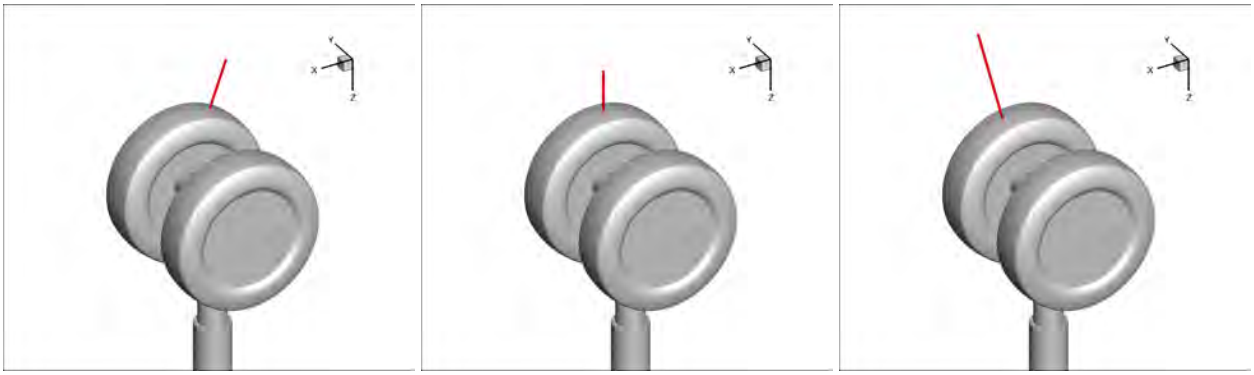


(g) Grid E, U (h) Grid E, V (i) Grid E, W



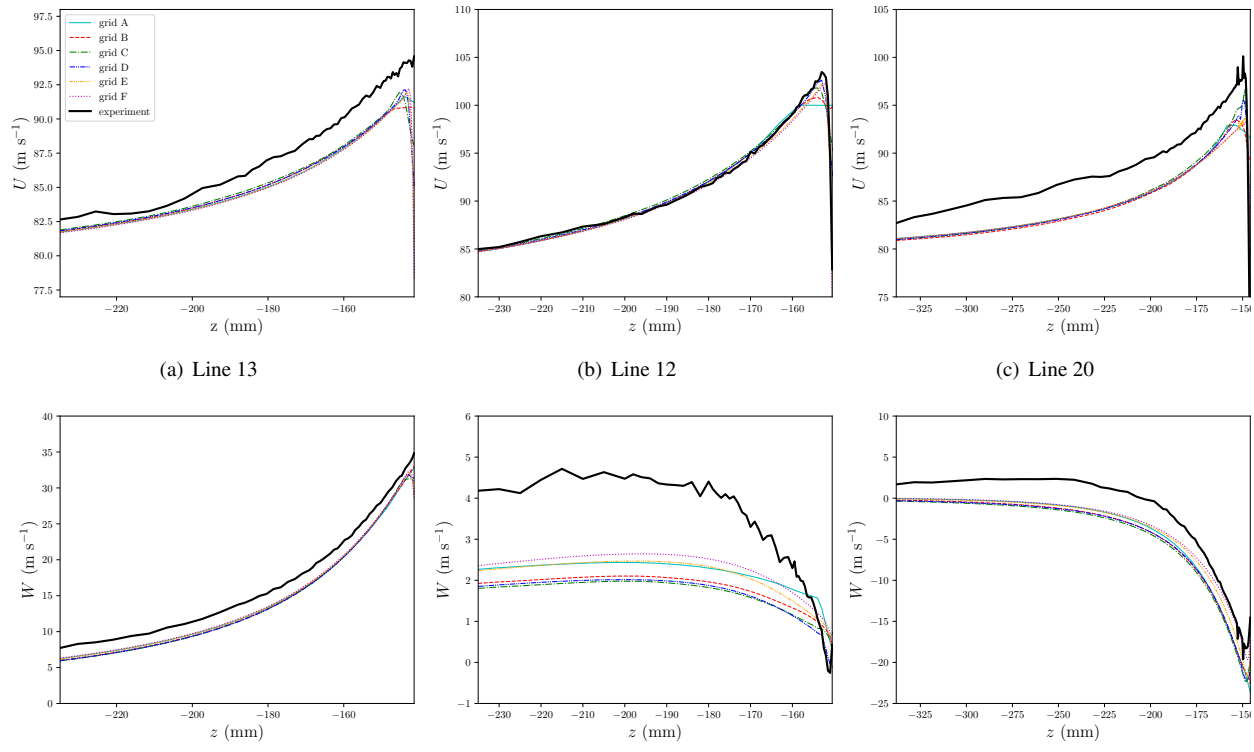
(j) Grid F, U (k) Grid F, V (l) Grid F, W

Fig. 12 Mean velocity field (in $\mathrm{m\ s^{-1}}$**) on a** x**-**y **plane downstream of the wheels at** $z = 0$ **for simulations without tripping strips.**



(a) Line 13 (b) Line 12 (c) Line 20

Fig. 13 Locations of 1D LDV measurement lines colored in red on the LAGOON landing gear. Left: line 13 that is upstream of line 12; right: line 20 that is downstream of line 12.



(a) Line 13 (b) Line 12 (c) Line 20

(d) Line 13 (e) Line 12 (f) Line 20

Fig. 14 Mean velocity components along different radial lines on the wheel surface showing the boundary layer profiles for simulations without tripping strips. Cyan solid line: grid A; red dashed line: grid B; green dash-dotted line: grid C; blue dash-dot-dotted line: grid D; orange dash-triple-dotted line: grid E; magenta dotted line: grid F; thick black solid line: experimental results.

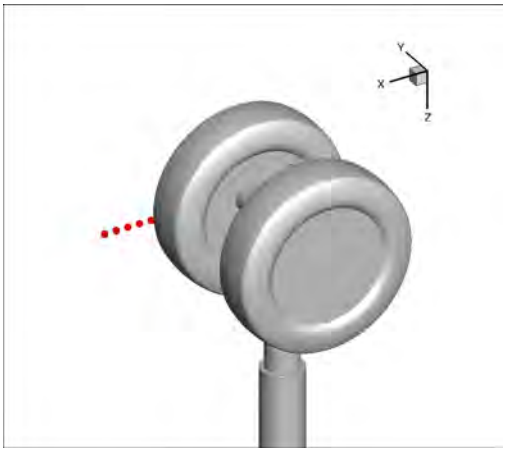
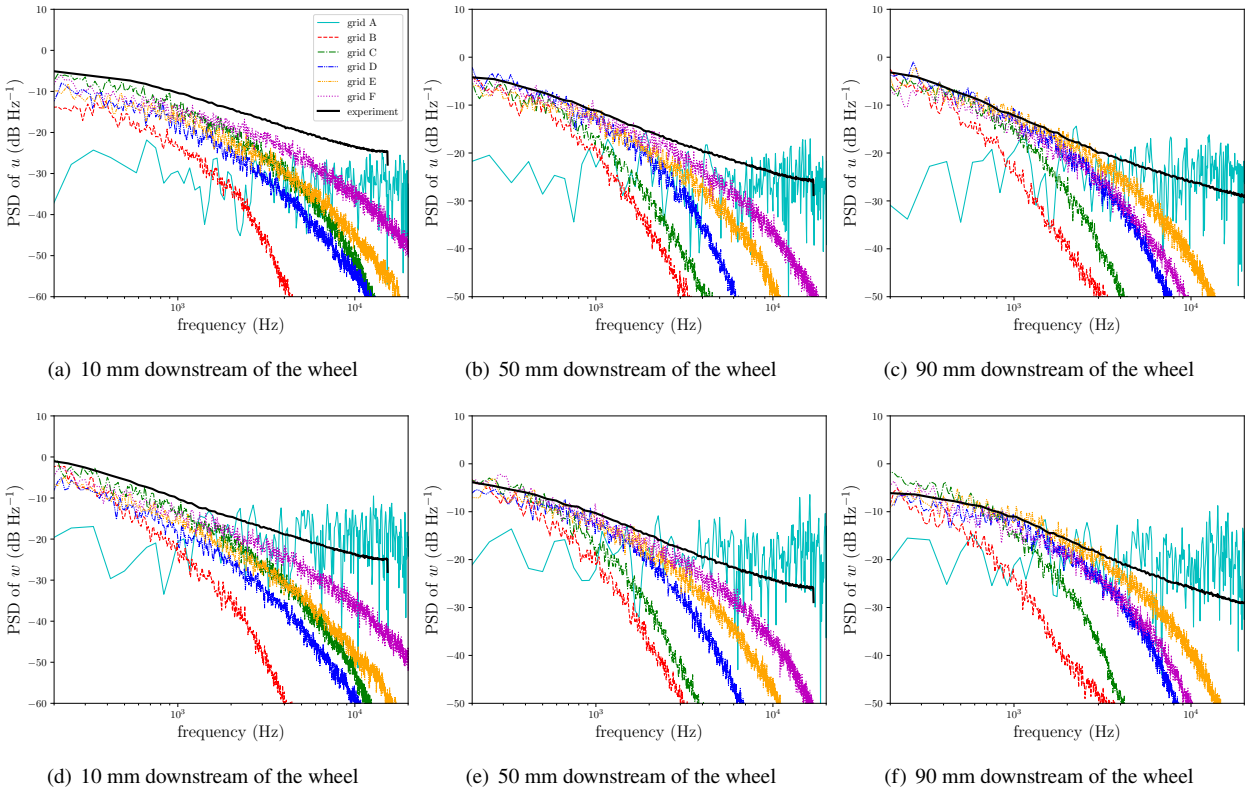


Fig. 15 The five LDV measurement locations at $y = -115$ mm and $z = 0$ along x direction from 10 mm to 90 mm downstream of the wheel.



(a) 10 mm downstream of the wheel (b) 50 mm downstream of the wheel (c) 90 mm downstream of the wheel

(d) 10 mm downstream of the wheel (e) 50 mm downstream of the wheel (f) 90 mm downstream of the wheel

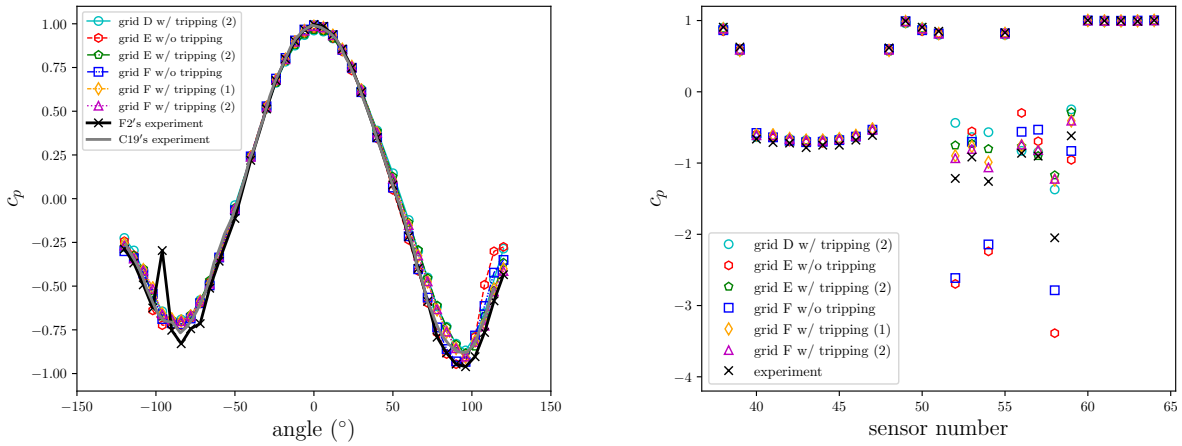
Fig. 16 Velocity PSDs at $y = -115$ mm and $z = 0$ at different locations downstream of the wheel for simulations without tripping strips. Cyan solid line: grid A; red dashed line: grid B; green dash-dotted line: grid C; blue dash-dot-dotted line: grid D; orange dash-triple-dotted line: grid E; magenta dotted line: grid F; thick black solid line: experimental results.

VI. Effects of Tripping Strips on Near-field Results

Simulation results with the effects of tripping devices included are studied in this section. The effects of the tripping devices are modeled by numerical tripping strips. The settings of the numerical tripping strips are discussed in an earlier section. Only the higher resolution grids, grids D, E, and F, are used for the simulations with numerical tripping. Four different combinations of grids and tripping cases are chosen for the presentation. These consist of grids D and E with only tripping case (2), and grid F with both tripping cases (1) and (2). It should be reminded that there are only numerical tripping strips at the axle and the main strut for case (1) while case (2) has tripping strips placed at all tripping locations in the experiments. The simulation results obtained from the grids E and F cases without the tripping strips are also included in the plots for comparison.

A. Mean Pressure Coefficients

The effects of the numerical tripping strips on the mean pressure coefficients are shown in Fig. 17. The comparison of mean pressure coefficients on the wheel periphery for different cases is shown in Fig. 17(a). There is no noticeable difference between all of the cases for the negative angles, i.e. on the bottom of the wheel, no matter with or without the numerical tripping strips. The main effects of the tripping are on the top of the wheel. In the favorable pressure gradient region on the top wheel, the pressure coefficients for cases with tripping strips start to deviate from the cases without tripping when the angle is greater than 60°. As a result, the c_p values are slightly over-predicted under the numerical tripping effects at these angles. The minimum c_p values for these tripping cases are closer to the C19's data. In the range of angles with adverse pressure gradients, the results with tripping effects included are less sensitive to grid resolution compared to those without tripping strips, and agree well with the experimental results from the C19 wind tunnel.



(a) Circular ring around the wheel

(b) Other locations

Fig. 17 Mean pressure coefficients on the LAGOON landing gear. Cyan circles (with solid line): grid D with tripping strips case (2); red hexagons (with dashed line): grid E without tripping strips; green pentagons (with dash-dotted line): grid E with tripping strips case (2); blue squares (with dash-dot-dotted line): grid F without tripping strips; orange diamonds (with dash-triple-dotted line): grid F with tripping strips case (1); magenta triangles (with dotted line): grid F with tripping strips case (2); black crosses (with thick solid line): experimental results of F2 wind tunnel; gray thick solid line: experimental results of C19 facility.

Fig. 17(b) compare the pressure coefficients at other sensor locations. Excluding the sensors on the axle and main strut that are in between #52-#64, there are insignificant differences between cases with and without the numerical tripping strips. Among the sensors on the axle and main strut, those which are around the front stagnation points, #51, #55, and #60-#64, agree perfectly with the experimental values. At other locations that are affected by the wake and the physical tripping devices, there are considerably less grid sensitivities in the c_p values, under the effects of numerical tripping, compared to cases without tripping shown in Fig. 10(b). It is very likely that the tripping devices in the experiments triggered turbulent transition further upstream of the boundary layer and this may avoid the need to

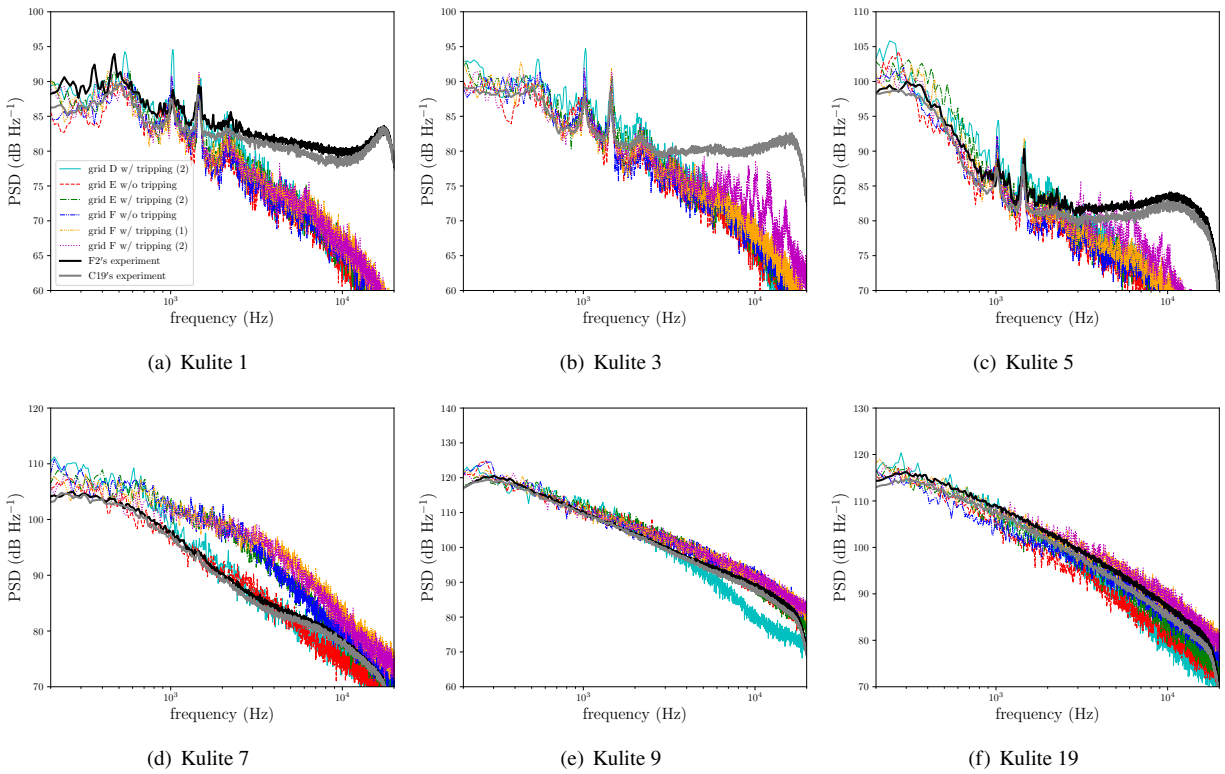
capture the complex flow phenomena around cylinders at sub-critical and critical Reynolds numbers in the computations. Overall, with the tripping effects modeled in the simulations, less grid sensitivities are achieved for mean pressure coefficients at sensors on the strut and axle, and there are better agreements of the c_p values between the simulations and experiments in general.

B. Pressure Power Spectral Densities

The effects of numerical tripping on the PSDs of pressure are studied from Figs. 18 to 20. The PSDs along the wheel periphery are shown in Fig. 18. From Fig. 18(a), it can be seen that there is no influence of the numerical tripping on the PSDs at Kulite 1 that is located right downstream of a tripping strip on the wheel. The numerical tripping strips on the wheels have more effects on PSDs at Kulites 3 and 5 by comparing the two tripping cases (1) and (2) with grid F. As shown in Figs. 18(b) and 18(c), the spectra at these two Kulites are excited to higher sound levels by the wheel tripping strips in the high frequency range although there are still quite large under-predictions compared to the experimental spectra in that range. The small influence on the boundary layers of the wheels' numerical tripping strips can already be seen in the comparison of visualizations between the grid F simulations in Fig. 7. The tripping effects in the experiments are challenging to reproduce due to the uncertainties of the small spatio-temporal scales involved and it is very likely that they are not fully modeled by our numerical tripping technique. At the Kulite 7, the PSDs seem to be quite sensitive to the flow separation location on the wheel and there is a larger sound level if the flow is predicted to separate at a more upstream location. The flow separation point is influenced by the wake behavior of the axle and strut which is sensitive to the grid resolution and the numerical tripping. With the tripping strips, it is interesting to see that the PSD obtained with grid D agrees much better with the experimental results. However, the tripping also causes over-prediction of the spectrum with grid E. As for the simulations with grid F, there are over-predictions in PSD no matter whether tripping is turned on or off. At Kulites 9 and 19 where the flow becomes fully turbulent, the PSDs obtained by the simulations with grids E and F have remarkably high accuracy for around two decades of frequencies, as shown in Figs. 18(e) and 18(f). Lower cutoff frequencies can be seen for the PSDs computed with grid D due to lower grid resolution. While there are not any noticeable effects from tripping at Kulite 9, small improvements with the numerical tripping strips are observed at Kulite 19 for both grids E and F.

The plots in Fig. 19 show the PSDs on the wheel internal and external sides. The PSDs at Kulite 10 located on the external side are found to be very sensitive to the grid resolution in the previous section. We should emphasize again that the experimental measurements also have quite large mismatch. Among all simulations without the numerical tripping, the PSD computed using grid E has the best agreement with the experimental PSD measured in the C19 facility. When tripping strips are placed on the wheel, the PSD spectrum from grid E is lifted up to match with the results from the F2 wind tunnel instead. The tripping effect, which is likely from the outer strips on the wheel, also improves PSD obtained with grid F and the corresponding PSD also has considerably good agreement with PSD from the F2 wind tunnel. At Kulite 11, the effects of tripping on the wheel can also be observed. The tripping strips on the wheel improve the PSD's computed with grids E and F in the low frequency range. However, there are still large under-predictions in the medium and high frequency ranges. The PSDs at the three consecutive Kulites, 13, 14, and 15 on the front part of the wheel's inner side are compared in Figs. 19(c) to 19(e). The effects of tripping are small at these three Kulites. The tripping does not affect the accurate capturing of the cavity tones in the PSDs at Kulites 13 to 15 but lead to slightly more over-predictions of the sound levels in the high frequency range. The Kulites 18 and 22 are placed at mirror locations on the rear and external sides of the two wheels. While good matches between the experimental results can be seen independently for these two Kulites, we have noticed that the experimental PSDs values at these two locations have around 5 dB difference in the low frequency range between 300 Hz and 2 kHz. The numerical tripping strips appear to have adverse effects on the PSDs computed with grid D at these Kulites. Nevertheless, the influence of tripping on the PSDs obtained with grids E and F is minor. In general, these PSDs compare well with the experimental results and the values in the low frequency range are in between the experimental results at the two mirror locations. As for another pair of Kulites, 20 and 21, which are also at mirror locations but on the rear and inner sides of the two wheels, the effects of tripping are not obvious. These two Kulites are inside the turbulent wake and their PSDs are reasonably captured using grids E and F with small over-predictions over a wide frequency range.

Finally, the PSDs at Kulites on the axle and strut are shown in Fig. 20. The improvements with the numerical tripping strips are tremendous at some of these Kulites. For example, the PSDs at Kulites 23 and 26, which are on the axle and the lower leg respectively, agree much better with the experimental results. The grid sensitivity is also small at these two locations. Kulite 25 is the only Kulite that is adversely affected as the PSD levels in the middle range of frequencies are over-predicted. Particularly, the two tonnes are not observable anymore for the grid F cases with



(a) Kulite 1 (b) Kulite 3 (c) Kulite 5

(d) Kulite 7 (e) Kulite 9 (f) Kulite 19

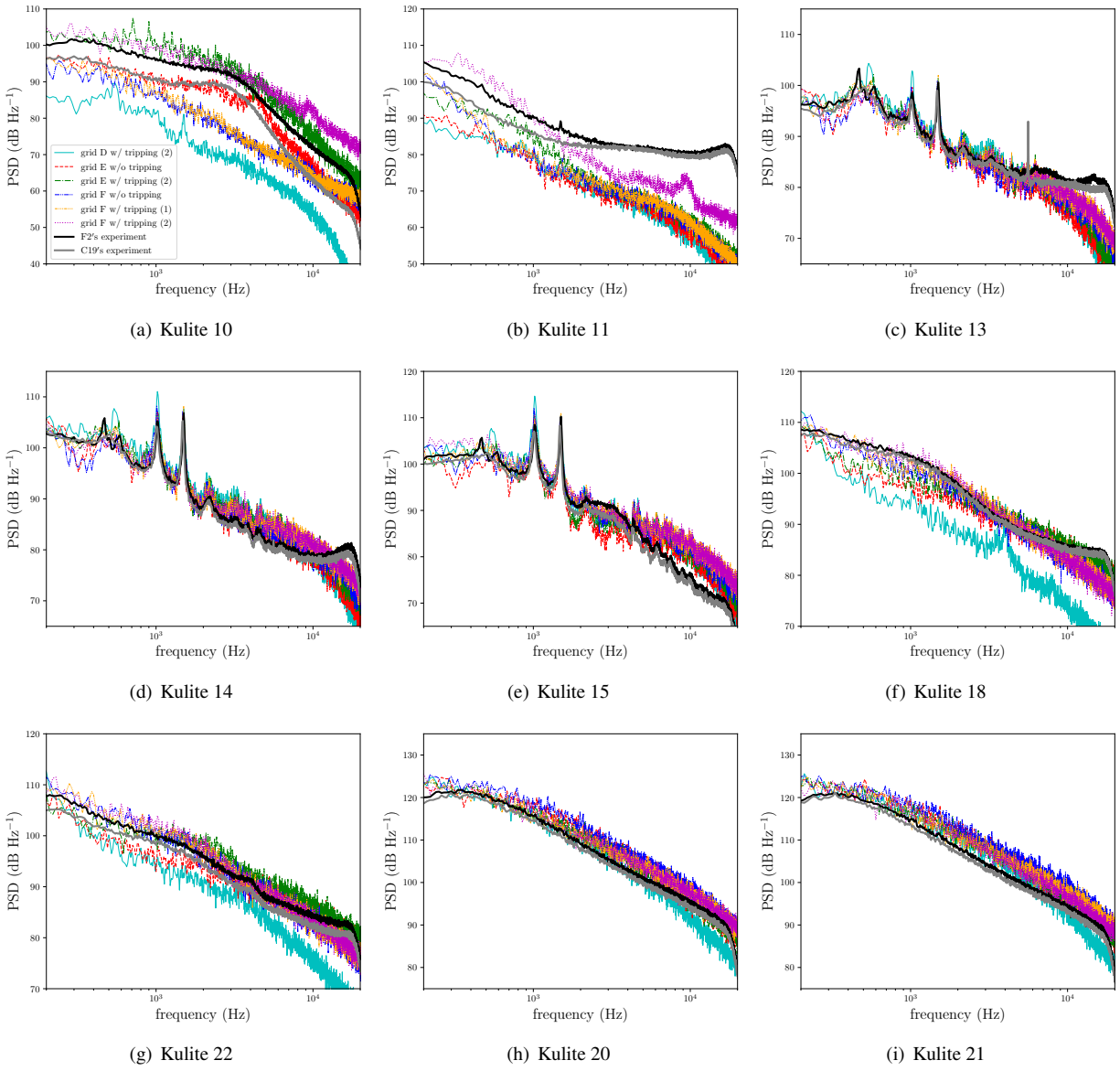
Fig. 18 Pressure PSDs at the wheel periphery. Cyan solid line: grid D with tripping strips case (2); red dashed line: grid E without tripping strips; green dash-dotted line: grid E with tripping strips case (2); blue dash-dot-dotted line: grid F without tripping strips; orange dash-triple-dotted line: grid F with tripping strips case (1); magenta dotted line: grid F with tripping strips case (2); black thick solid line: experimental results of F2 wind tunnel; gray thick solid line: experimental results of C19 facility.

tripping strips. The numerical tripping also improves PSDs predicted by simulations with different grids generally at Kulite 27, where the flow is supposed to be fully turbulent.

C. Mean Velocity Fields

In Fig. 21, the mean velocity components from different cases using grid F are compared. It can be seen that the numerical tripping strips have strong effects on the wake topology although the effects mainly originate from the tripping on the axle and strut and not on the wheels. This can be easily deduced by comparing the velocity profiles between tripping cases (1) and (2), which are very similar. With the numerical tripping, there are much better agreements in the mean velocity profiles between the simulation and experimental results. From the plots of mean streamwise velocity U, it can be observed that the contours in region around the core of the wake and close to the landing gear are better reproduced with more streamwise momentum deficit. The magnitudes of the mean transverse velocity component V are also closer to those measured from the experiments. The mean vertical velocity component W contours are less positive in the center of the wake near the landing gear but this behavior cannot be fully validated due to incomplete experimental data in that region. The grid sensitivities of simulations that belong to the case (2) of numerical tripping are compared in Fig. 22. Much less grid sensitivities are observed in the plots, compared to the earlier comparison of simulations without numerical tripping. Simulations with different grids can all capture the low magnitude region of U in the middle right downstream of the landing gear. When the grid is refined, there seems to be a trend to converge to the experimental results. Overall, these results strongly suggest that the modeling of the laminar-turbulent transition induced by the tripping devices on the axle and strut is critical in these WMLESs for reproducing the correct wake topology from the experiments.

The tripping effects on the mean velocity profiles around the periphery of the wheels are shown in Fig. 23. The



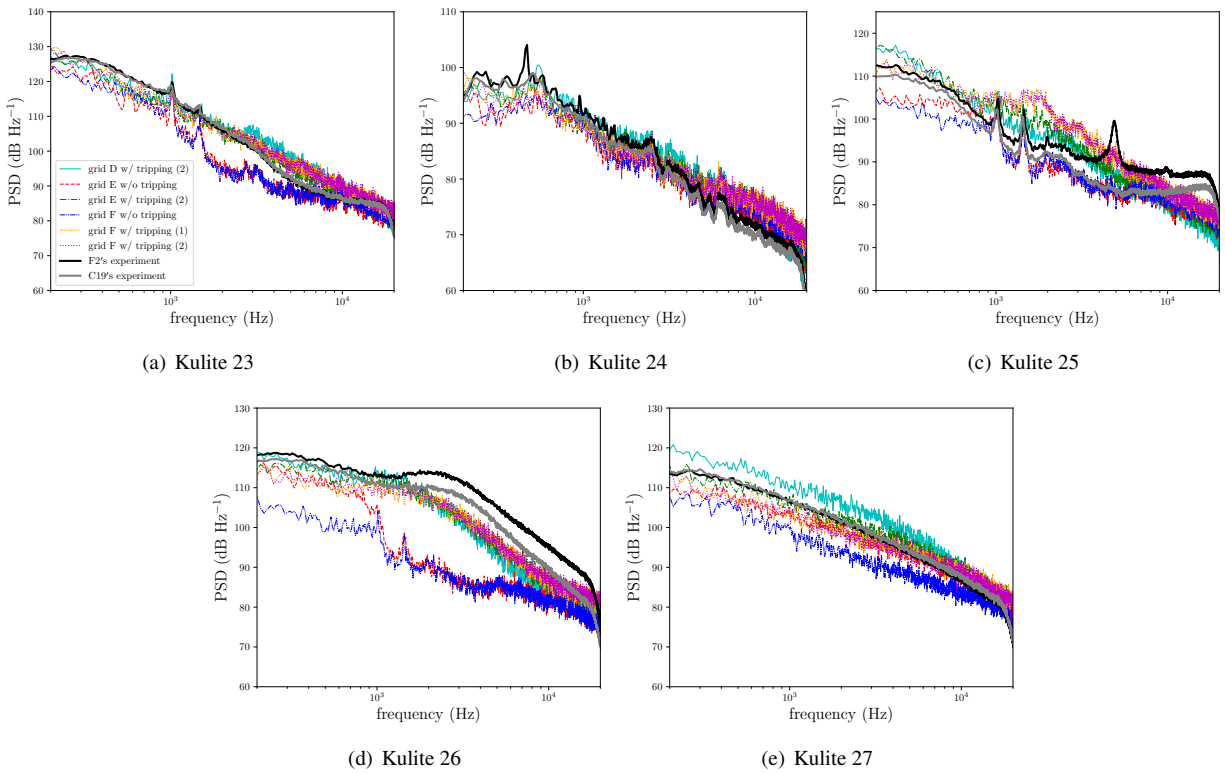
(a) Kulite 10 (b) Kulite 11 (c) Kulite 13

(d) Kulite 14 (e) Kulite 15 (f) Kulite 18

(g) Kulite 22 (h) Kulite 20 (i) Kulite 21

Fig. 19 Pressure PSDs at the wheel internal and external sides. Cyan solid line: grid D with tripping strips case (2); red dashed line: grid E without tripping strips; green dash-dotted line: grid E with tripping strips case (2); blue dash-dot-dotted line: grid F without tripping strips; orange dash-triple-dotted line: grid F with tripping strips case (1); magenta dotted line: grid F with tripping strips case (2); thick black line: experimental results of F2 wind tunnel; thick gray line: experimental results of C19 facility.

effects of tripping strips, mainly come from those on the axle and strut, increase the magnitudes of W quite significantly. As a result, W obtained from cases with tripping agree better with the experimental results. Meanwhile, the magnitudes of U are also reduced and deviate more from the experimental measurements because of tripping. Nevertheless, these additional deviations from the experimental results are small compared to the considerably large discrepancies between the simulation and experimental results for cases without tripping originally. As explained in the earlier section, the under-estimation of U is believed to be caused by the use of an open domain in the simulations where the blockage effects in the F2 wind tunnel are not accounted for.



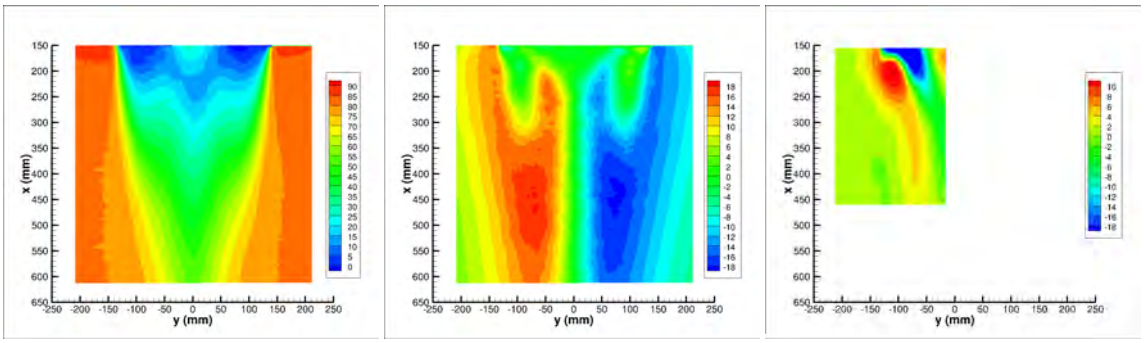
(a) Kulite 23 (b) Kulite 24 (c) Kulite 25

(d) Kulite 26 (e) Kulite 27

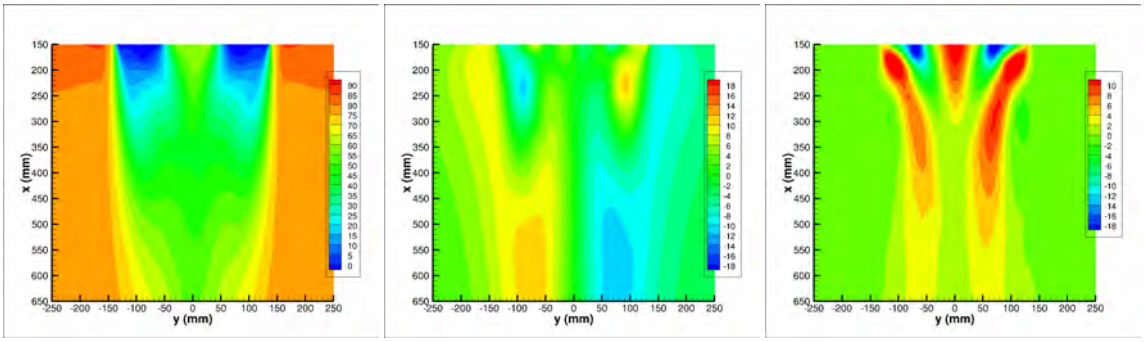
Fig. 20 Pressure PSDs at the axle and lower strut. Cyan solid line: grid D with tripping strips case (2); red dashed line: grid E without tripping strips; green dash-dotted line: grid E with tripping strips case (2); blue dash-dot-dotted line: grid F without tripping strips; orange dash-triple-dotted line: grid F with tripping strips case (1); magenta dotted line: grid F with tripping strips case (2); thick black line: experimental results of F2 wind tunnel; thick gray line: experimental results of C19 facility.

D. Velocity Power Spectral Densities

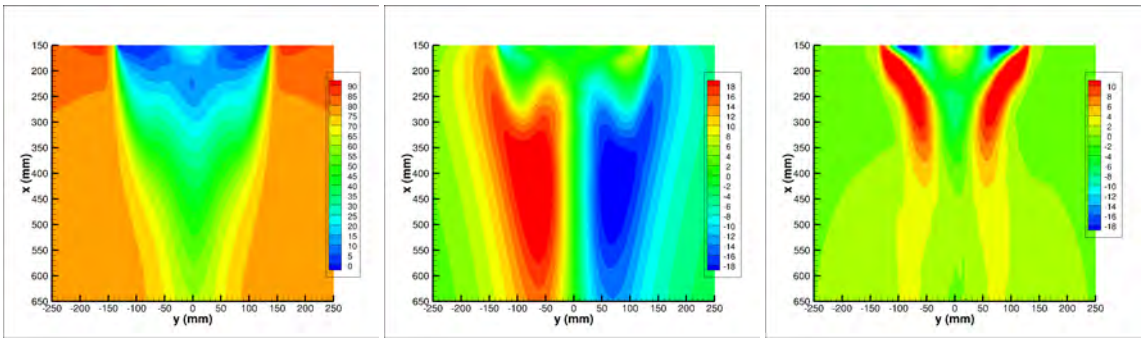
The effects of the numerical tripping on the velocity PSD can be studied from Fig. 24. With the tripping strips, the cut-off frequencies of the PSDs are higher and this is mainly caused by the tripping on the axle and strut. However, there is still mismatch in the low frequency PSD levels at the probe that is closest to the wheel, even with the numerical tripping. At other probing locations, the spectra from the simulations with grids E and F agree well with those from the experiments for almost one decade of frequency range with the effects of numerical tripping.



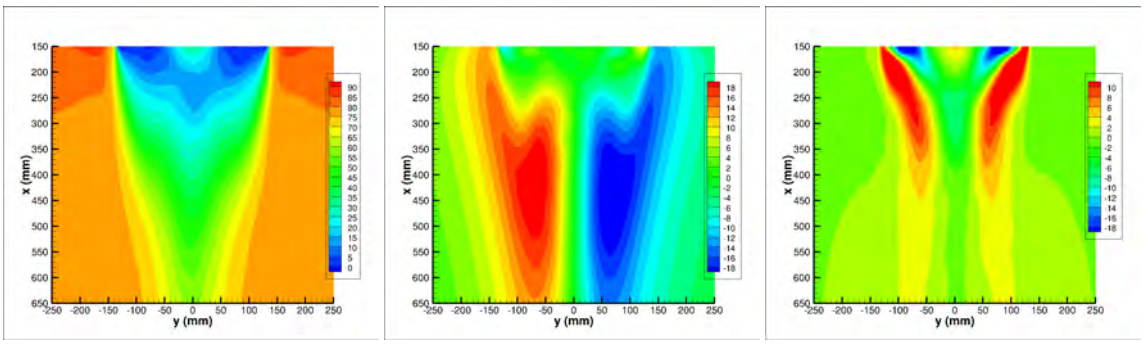
(a) Experiment, U (b) Experiment, V (c) Experiment, W



(d) Grid F without tripping strips, U (e) Grid F without tripping strips, V (f) Grid F without tripping strips, W

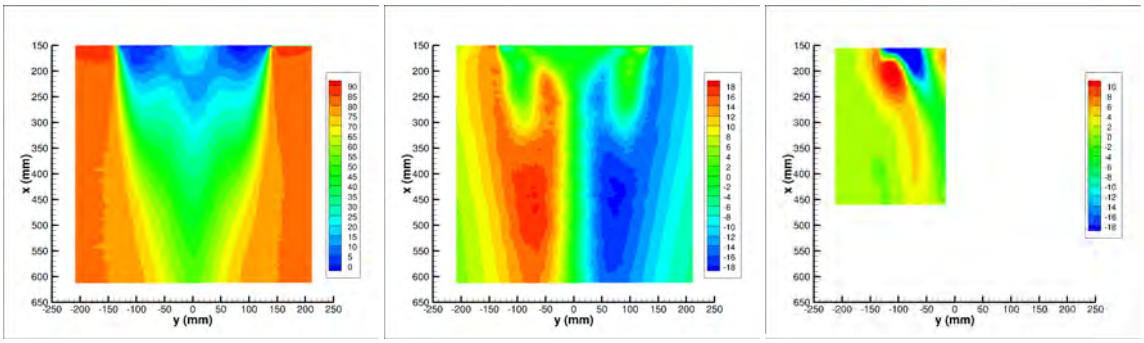


(g) Grid F with tripping strips case (1), U (h) Grid F with tripping strips case (1), V (i) Grid F with tripping strips case (1), W

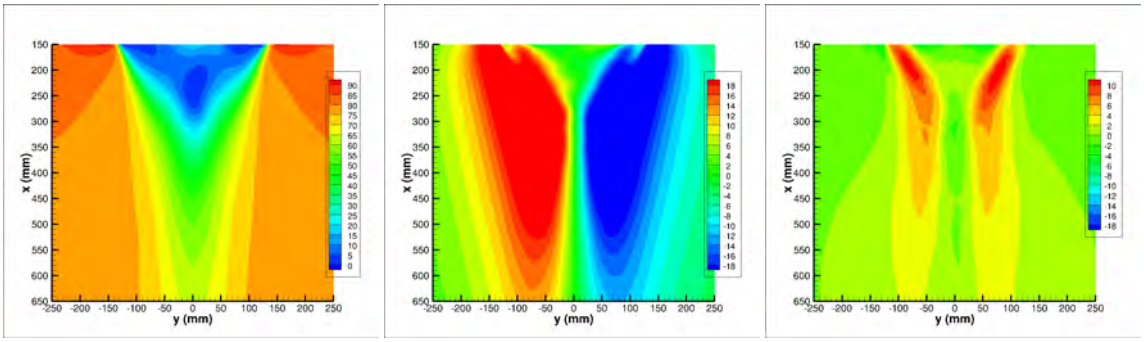


(j) Grid F with tripping strips case (2), U (k) Grid F with tripping strips case (2), V (l) Grid F with tripping strips case (2), W

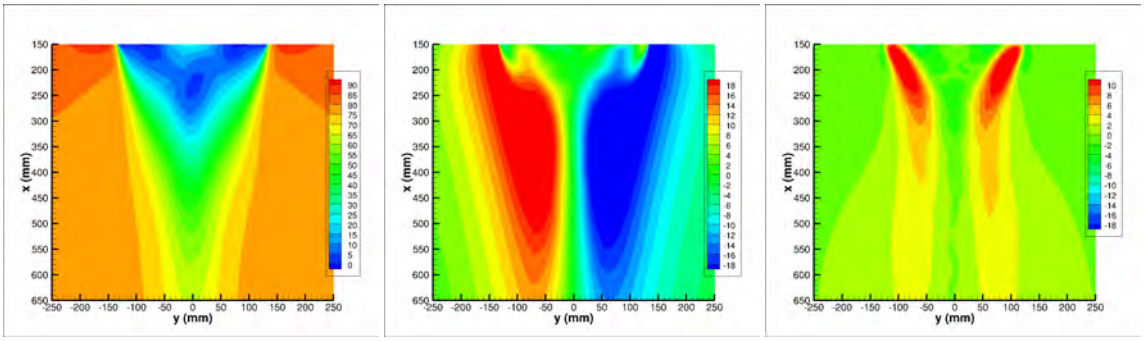
Fig. 21 Mean velocity field (in m s^{-1}) on a x-y plane downstream of the wheels at $z = 0$ of different simulations with grid F.



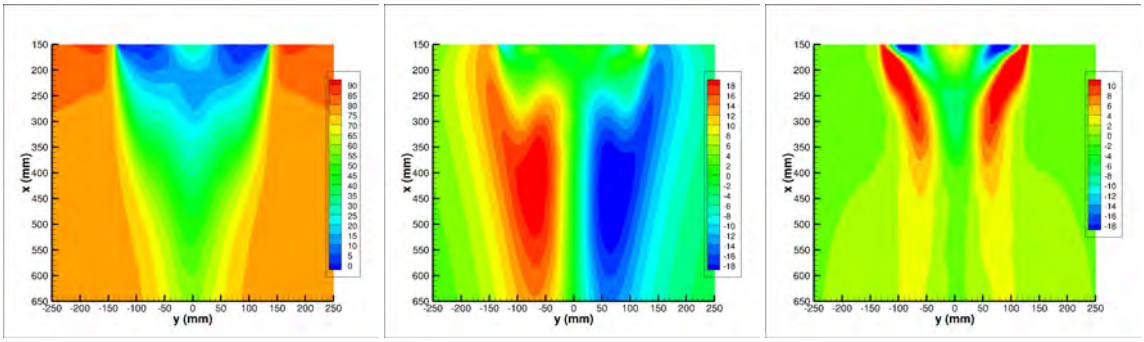
(a) Experiment, U (b) Experiment, V (c) Experiment, W



(d) Grid D with tripping strips case (2), U (e) Grid D with tripping strips case (2), V (f) Grid D with tripping strips case (2), W

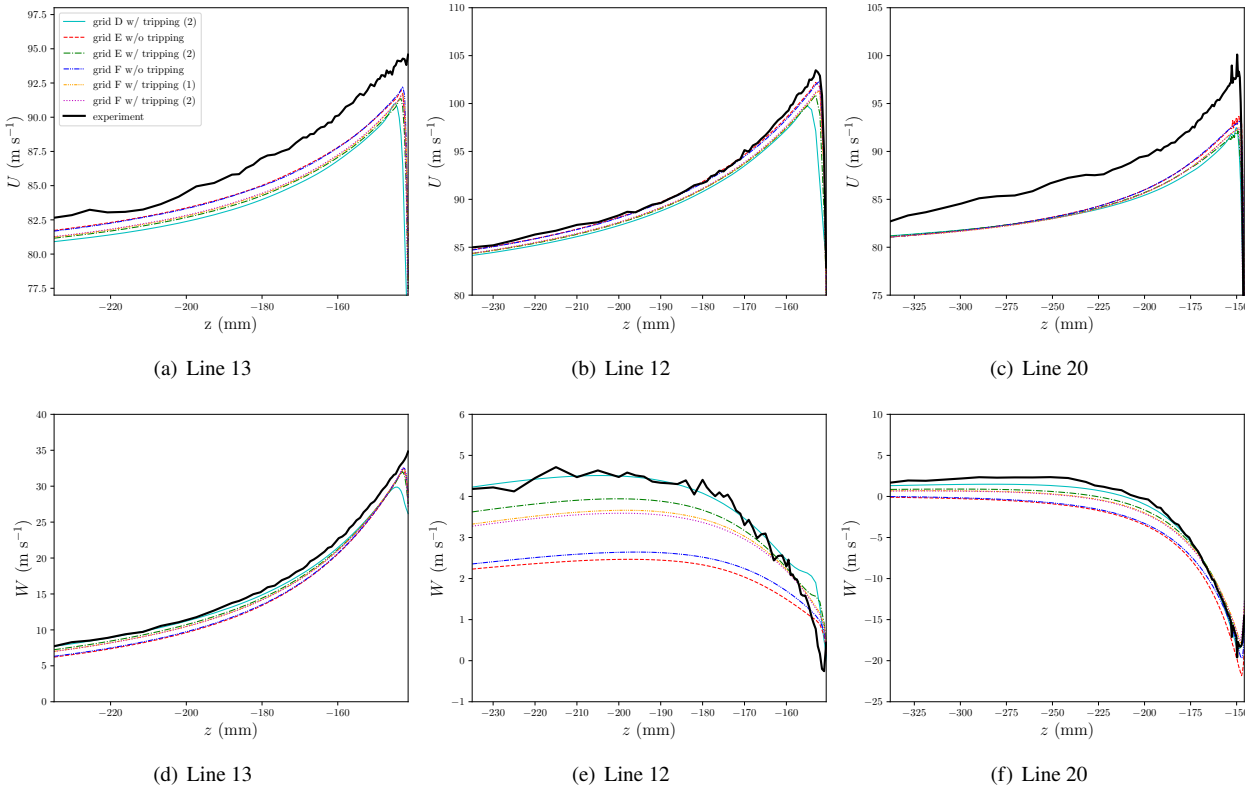


(g) Grid E with tripping strips case (2), U (h) Grid E with tripping strips case (2), V (i) Grid E with tripping strips case (2), W



(j) Grid F with tripping strips case (2), U (k) Grid F with tripping strips case (2), V (l) Grid F with tripping strips case (2), W

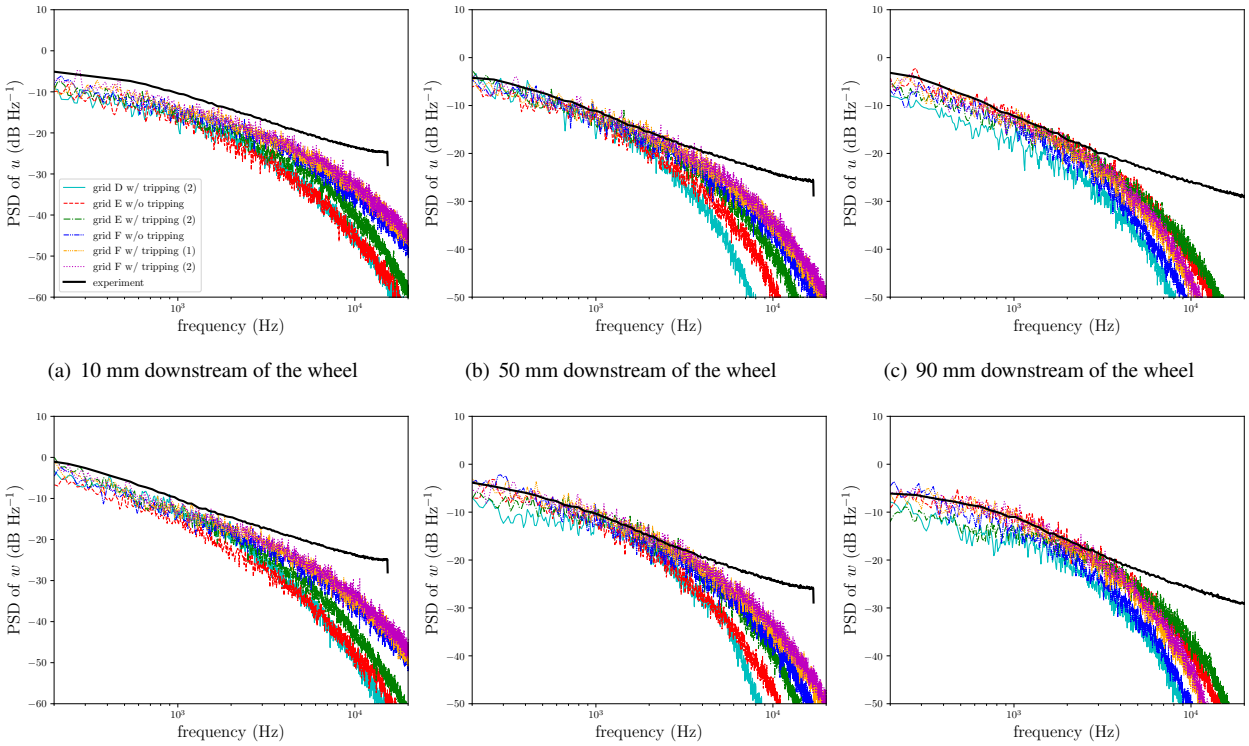
Fig. 22 Mean velocity field (in m s^{-1}) on a x-y plane downstream of the wheels at $z = 0$ of different simulations with tripping strips case (2).



(a) Line 13 (b) Line 12 (c) Line 20

(d) Line 13 (e) Line 12 (f) Line 20

Fig. 23 Mean velocity components along different radial lines on the wheel surface showing the boundary layer profiles. Cyan solid line: grid D with tripping strips case (2); red dashed line: grid E without tripping strips; green dash-dotted line: grid E with tripping strips case (2); blue dash-dot-dotted line: grid F without tripping strips; orange dash-triple-dotted line: grid F with tripping strips case (1); magenta dotted line: grid F with tripping strips case (2); thick black solid line: experimental results.



(a) 10 mm downstream of the wheel (b) 50 mm downstream of the wheel (c) 90 mm downstream of the wheel

(d) 10 mm downstream of the wheel (e) 50 mm downstream of the wheel (f) 90 mm downstream of the wheel

Fig. 24 Velocity PSDs at $y = -115$ mm and $z = 0$ at different locations downstream of the wheel. Cyan solid line: grid D with tripping strips case (2); red dashed line: grid E without tripping strips; green dash-dotted line: grid E with tripping strips case (2); blue dash-dot-dotted line: grid F without tripping strips; orange dash-triple-dotted line: grid F with tripping strips case (1); magenta dotted line: grid F with tripping strips case (2); thick black solid line: experimental results.

VII. Far-field Acoustic Predictions

The Ffowcs Williams–Hawkings (FWH) acoustic analogy [56] is applied to estimate the far-field noise with the near-field CFD data. Consider a moving body immersed in a fluid with quiescent ambient state, the FWH equation for a permeable surface described by $f(\boldsymbol{x}, t) = 0$ is given by [57]

$$\Box^2 \left(c_0^2 \rho'\right) = \frac{\partial}{\partial t}\left[Q_n \delta\left(f\right)\right] - \frac{\partial}{\partial x_i}\left[L_i \delta f\right] + \frac{\partial^2}{\partial x_i \partial x_j}\left[T_{ij} H\left(f\right)\right], \tag{3}$$

where $Q_n = Q_i \hat{n}_i$ and $L_i = L_{ij} \hat{n}_j$. Q_i and L_{ij} are defined as

$$Q_i = \rho_0 v_i + \rho\left(u_i - v_i\right), \tag{4}$$

$$L_{ij} = P'_{ij} + \rho u_i \left(u_j - v_j\right). \tag{5}$$

$\Box^2 = c_0^{-2}\partial^2/\partial t^2 - \nabla^2$ is the wave operator with the ambient sound speed c_0. f is normalized in a way such that $|\nabla f| = 1$. As a result, $\boldsymbol{n} = \nabla f$ is the outward unit vector normal to the FWH surface. $H(f)$ is the Heaviside function and $\delta f = H'(f)$ is the Dirac delta function. $\rho' = \rho - \rho_0$ is the fluctuation of the density ρ from the ambient density $\rho_0 = \rho_\infty$. u_i and v_i are the velocities of the fluid and the surface respectively. $P'_{ij} = P_{ij} - p_0 \delta_{ij}$ is the perturbation compressible stress tensor where $p_0 = p_\infty$ is the ambient pressure and δ_{ij} is the Kronecker delta. The compressible stress tensor P_{ij} and the Lighthill stress tensor T_{ij} are given by

$$P_{ij} = p\delta_{ij} - \tau_{ij}, \tag{6}$$

$$T_{ij} = \rho u_i u_j + P'_{ij} - c_0^2 \rho' \delta_{ij}, \tag{7}$$

where p and τ_{ij} are the pressure and viscous stress tensor respectively. Note that Equation (3) is an exact rearrangement of the density and momentum equations of the Navier–Stokes equations.

The integral solution of Equation (3) for the acoustic pressure or pressure fluctuation, $p' = p - p_0$, at the observer position $\boldsymbol{x}$ and observer time t can be derived using the free-space Green's function:

$$c_0^2 \rho'^2\left(\boldsymbol{x}, t\right) = p'\left(\boldsymbol{x}, t\right) = p'_T\left(\boldsymbol{x}, t\right) + p'_L\left(\boldsymbol{x}, t\right) + p'_Q\left(\boldsymbol{x}, t\right), \tag{8}$$

where $p'_T\left(\boldsymbol{x}, t\right)$, $p'_L\left(\boldsymbol{x}, t\right)$, and $p'_Q\left(\boldsymbol{x}, t\right)$ are the thickness, loading, and quadrupole terms respectively. The left equality $p' = c_0^2 \rho'^2$ comes from the assumption that the observer is sufficiently far away from the acoustic source region and the fluctuations are small.

In this study, the solid (impermeable) FWH approach with the FWH surface placed on the landing gear is adopted since the results obtained with the solid FWH formulation are in general better than those of the permeable FWH approach in the BANC workshop [17]. Moreover, the placement of the FWH surface is more challenging in the permeable FWH approach. With the solid FWH formulation, Q_n and L_i are reduced to

$$Q_n = \rho_0 v_i \hat{n}_i, \tag{9}$$

$$L_i = P'_{ij} \hat{n}_j, \tag{10}$$

due to no-penetration conditions. One of the derived solutions of thickness and loading noise components with solid FWH surface are given by the Formulation 1A [28, 58]. The corresponding integral solutions over the surface S are given by

$$4\pi p'_T\left(\boldsymbol{x}, t\right) = 4\pi c_0^2 \rho'_T\left(\boldsymbol{x}, t\right) = \int_{f=0} \left[\frac{Q_n c_0 \left(M_R - M^2\right)}{R^2 \left|1 - M_R\right|^3}\right]_{ret} dS, \tag{11}$$

$$\begin{aligned} 4\pi p'_L\left(\boldsymbol{x}, t\right) = 4\pi c_0^2 \rho'_L = {} & \frac{1}{c_0}\int_{f=0} \left[\frac{\dot{L}_R}{R\left|1 - M_R\right|^2}\right]_{ret} dS \\ & + \int_{f=0} \left[\frac{L_R - L_M}{R^2 \left|1 - M_R\right|^2}\right]_{ret} dS \\ & + \int_{f=0} \left[\frac{L_R \left(M_R - M^2\right)}{R^2 \left|1 - M_R\right|^3}\right]_{ret} dS. \end{aligned} \tag{12}$$

It is assumed that the solid surface is in uniform rectilinear motion when the solutions above are derived. The subscript "ret" denotes integration at the retarded or emission time τ of the surface elements. $M_i = v_i/c_0$ is the Mach number vector of the moving surface. Other terms in the solutions are defined as

$$M^2 = M_i M_i, \quad M_R = M_i \hat{R}_i, \tag{13}$$

$$L_R = L_i \hat{R}_i, \quad L_M = L_i M_i, \quad \dot{L}_R = \frac{\partial L_i}{\partial \tau} \hat{R}_i, \tag{14}$$

where $R = |\boldsymbol{x} - \boldsymbol{y}|$ is the acoustic distance between the observer and the source (any surface element) at the retarded time and $\boldsymbol{R} = \nabla R/|\nabla R|$ is the unit radiation vector.

In a wind tunnel configuration, the problem can be further simplified by assuming the flow is in the x_1 direction with speed U_0 and Mach number M_0. For subsonic flow, the Garrick triangle [59–61] can be used to compute the retarded time and the acoustic distance since both the observer and source move at the same velocity. By the change of reference frame from the wind tunnel frame to the frame of the fluid at rest, Q_n can be further simplified as

$$Q_n = -\rho_0 U_0 \hat{n}_1. \tag{15}$$

The quadrupole component p'_Q requires volume integration of the quadrupole term (last term in the right hand side of Equation (3)) outside the FWH surface and is neglected for this low Mach number problem. The viscous stress tensor τ_{ij} in P_{ij} is also neglected as it is generally a negligible source of noise.

The FWH method presented is a time domain approach. One can also consider the frequency domain approach [60] with the use of fast Fourier transform (FFT). We have verified that both approaches give essentially the same numerical results.

The far-field noise was measured in the open jet C19 wind tunnel on two circular arcs located in a flyover plane and a sideline plane respectively with the origin at the landing gear. As depicted in Fig. 25, the sideline plane makes an angle of 56° with respect to the flyover plane and 12 microphones are evenly distributed on each arc from 30° (downstream) to 140° (upstream). The distance between the arcs' origin and the microphones is roughly $20D = 6$ m. The measured noise levels at these microphones, or observers, are corrected from the effects of background wind tunnel noise and the atmospheric absorption. The positions of the observers for far-field computations are also adjusted to take the refraction of acoustic propagation at the shear layer generated from the nozzle jet into account [30].

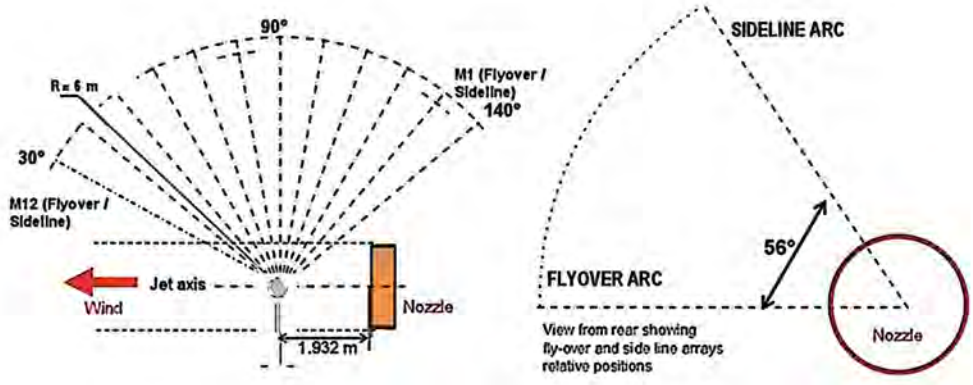


Fig. 25 Schematic showing the two arcs of 12 far-field microphones in flyover and sideline directions (part of the LAGOON database, property of Airbus/ONERA [30]).

From Fig. 25, we can see that the observers are not inside the jet and the flow is only at the freestream velocity in regions around the landing gear. As argued in [55], a large portion of the acoustic propagation is in the quiescent medium. Therefore, an ambient Mach number of $M_0 = 0$ is used in the FWH solver. The non-uniform effects of the flow past the landing gear are already included in the surface pressure obtained from the CFD simulations. Following the experiments, a bin frequency of 10 Hz is used for computing the PSD spectra at all observer locations with the Hann windowing and 75% overlap. The sampling frequency is 132 kHz.

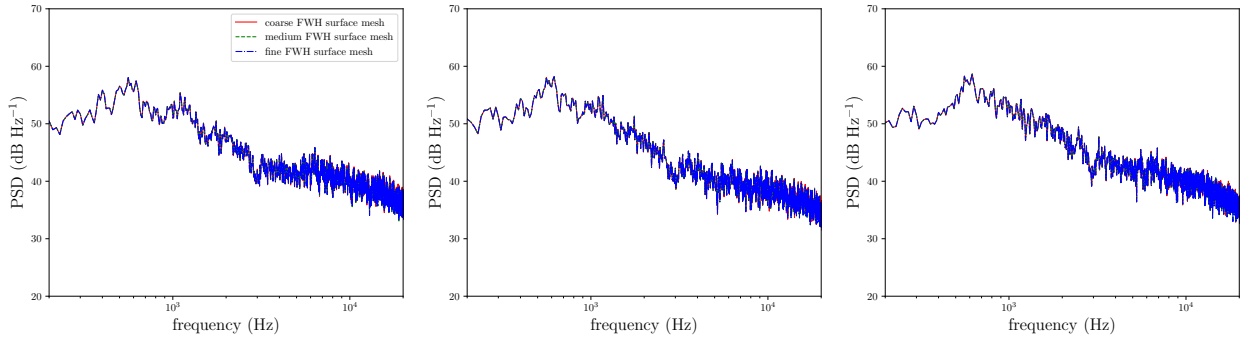
A. Surface Mesh Sensitivity Analysis of the Ffowcs Williams–Hawkings Analogy

The surface triangulations used for the FWH surface are different than those used for the immersed boundary method. A mesh resolution sensitivity study on the FWH surface is performed with three different surface triangulations described in Table 3. The far-field pressure PSDs computed with different FWH surface triangulations at a few observer locations are shown in Fig. 26. The case chosen is the simulation on grid F without tripping. From the plots, no noticeable differences between the PSDs are observed between results from different FWH surface triangulations. This indicates that a surface triangulation much coarser than that for the immersed boundary method can be used for data compression during the sampling of FWH surface data.

In the following sections, the data collected on the fine resolution FWH surface mesh is utilized for far-field noise predictions for simulations with grids D, E, and F, whereas data sampled on the medium resolution surface mesh is used for other lower resolution simulations.

Mesh	Surface element spacing (mm)	Number of surface elements (million)
coarse	~ 0.125	0.360
medium	~ 0.250	1.451
fine	~ 0.500	5.763

Table 3 The details of surface triangulations used for FWH surface.



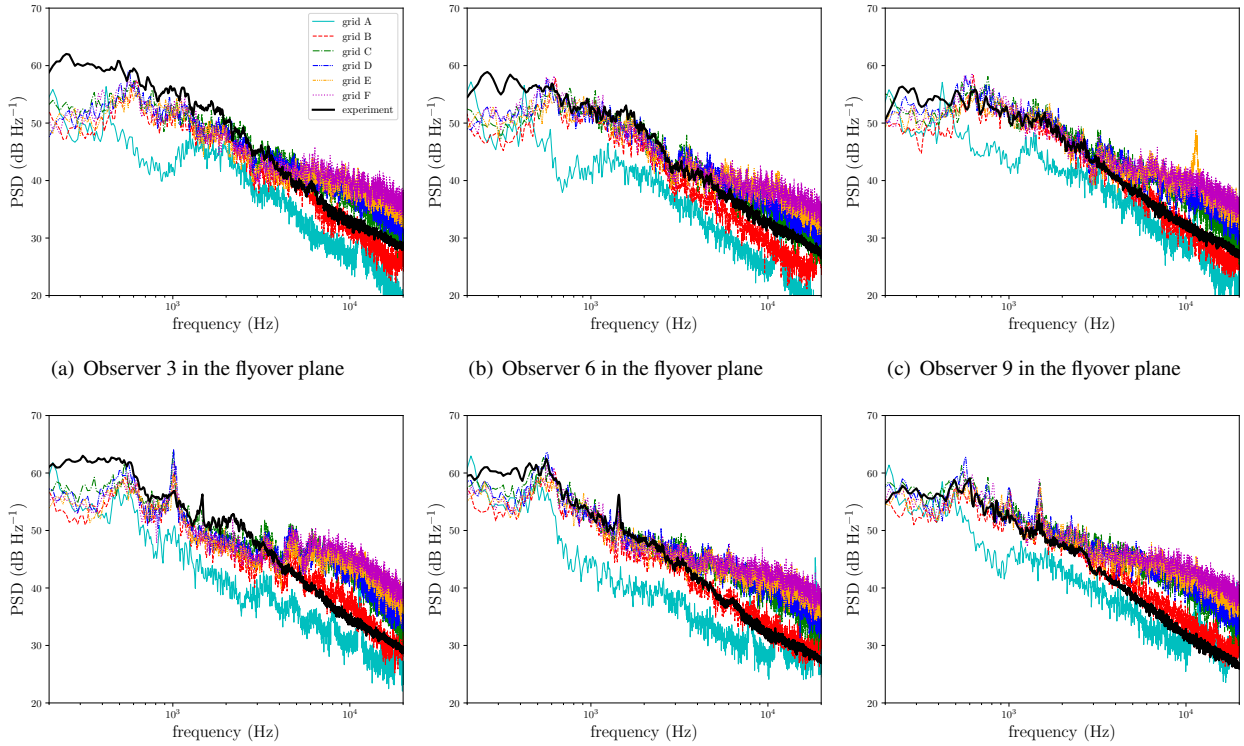
(a) Observer 3 in the flyover plane (b) Observer 6 in the flyover plane (c) Observer 9 in the flyover plane

Fig. 26 Sensitivity of surface mesh resolution on pressure PSDs of far-field noise at different locations of observers (microphones) using simulation results with grid F without tripping strips. Red solid line: coarse surface mesh; green dashed line: medium surface mesh; blue dash-dotted line: fine surface mesh.

B. Far-field Acoustic Results

The far-field acoustic predictions using the FWH surface data from different cases without the tripping strips are compared in Fig. 27. The results from grid A are excluded in the following discussion due to poor CFD grid resolution. For observer 9 that is located downstream of the landing gear, it can be seen from the plots that all numerical predictions compare reasonably well with the experimental results from 200 Hz to 4 kHz on both flyover and sideline planes. At other observer locations that are upstream of observer 9, there are under-predictions in the noise levels below 500 Hz and the under-estimation increases when the observer is at a more upstream location. This discrepancies were also reported in [15] and these may be caused by unexpected wind tunnel noise, or noise diffraction at the nozzle lip since these observers are closer to the jet nozzle. Two tonal peaks at around 1 kHz and 1.5 kHz are observed on the sideline plane in the experiments due to the radiation of the noise generated by cavity resonances to far-field and the latter is more visible than the former. These tonal peaks are also captured reasonably well by the simulations on the sideline plane. While noise levels below 4 kHz are fairly well predicted by the computations, over-predictions are observed in the higher frequency range from most of the simulations. In addition, the over-predictions are larger on the sideline

plane than on the flyover plane. The numerical results from the low resolution grid B agree surprisingly well with the experimental measurements in the high frequency range at most observer locations even though the wall pressure PSDs are under-predicted substantially at all Kulite locations in the same frequency range. The same contradiction was also found in the BANC workshop [17]. From the workshop results, the far-field predictions from simulations with different numerical and modeling approaches fit the experimental results well to more than 10 kHz using the solid FWH formulation, while the corresponding wall pressure PSD spectra are under-predicted below 2 kHz in general. This kind of contradiction is speculated to be caused by error cancellation in the integrals of the solid FWH formulation by Spalart et al. [62]. The over-predictions in the high frequency range from the higher resolution results may also be caused by the inaccuracy of the solid FWH formulation, given that the near-field predictions in the high frequency range with these grids, such as grids E and F, are much better than those with grid B.



(a) Observer 3 in the flyover plane

(b) Observer 6 in the flyover plane

(c) Observer 9 in the flyover plane

(d) Observer 3 in the sideline plane

(e) Observer 6 in the sideline plane

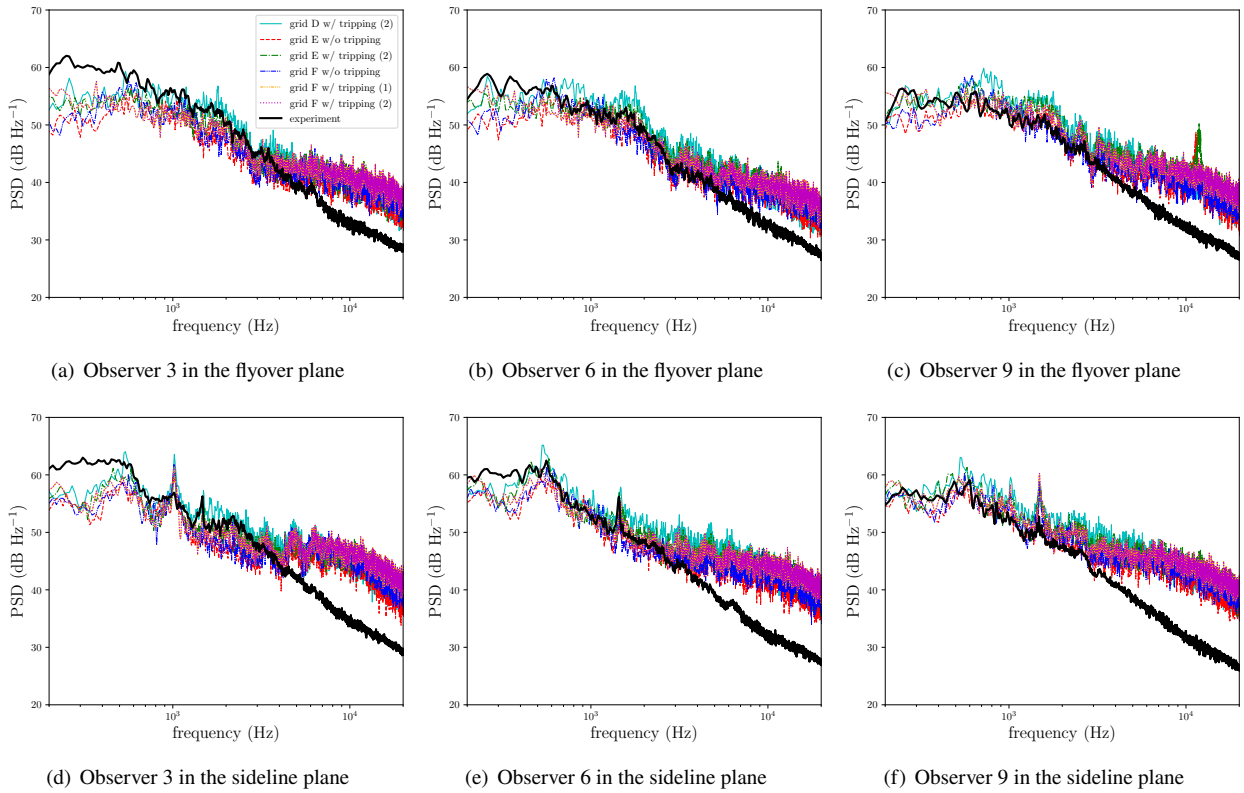
(f) Observer 9 in the sideline plane

Fig. 27 Pressure PSDs of far-field noise at different locations of observers (microphones) without effects of tripping strips. Cyan solid line: grid A; red dashed line: grid B; green dash-dotted line: grid C; blue dash-dot-dotted line: grid D; orange dash-triple-dotted line: grid E; magenta dotted line: grid F; thick black line: experimental results.

The effects of tripping on the far-field noise predictions are studied in Fig. 28. The numerical tripping has insignificant effects on the low frequency noise. In general, slightly more over-predictions in the high frequency range can be observed with tripping but the extra amount of over-predictions is small compared to those from the computations without tripping in the same frequency range.

VIII. Conclusion

The near-field flow and far-field noise generated from the flow past a simplified nose landing gear were simulated using different Cartesian octree grids, with finest grid spacings ranging from 4.8 mm to 0.2 mm. The simulations were conducted with and without the numerical modeling of the tripping devices installed on the landing gear in the experiments. Without the effects of the numerical tripping accounted, large grid sensitivities in the mean and unsteady near-field flow quantities were found at some regions near the axle and main strut, and the wake. While mean



(a) Observer 3 in the flyover plane

(b) Observer 6 in the flyover plane

(c) Observer 9 in the flyover plane

(d) Observer 3 in the sideline plane

(e) Observer 6 in the sideline plane

(f) Observer 9 in the sideline plane

Fig. 28 Effects of tripping strips on pressure PSDs of far-field noise at different locations of observers (microphones). Cyan solid line: grid D with tripping strips case (2); red dashed line: grid E without tripping strips; green dash-dotted line: grid E with tripping strips case (2); blue dash-dot-dotted line: grid F without tripping strips; orange dash-triple-dotted line: grid F with tripping strips case (1); magenta dotted line: grid F with tripping strips case (2); thick black line: experimental results.

pressure coefficients around the wheels have good agreements with the experimental results, large grid sensitivities and discrepancies with the experimental values were observed at many other locations on the axle and main strut. The large grid sensitivities of the mean pressure around the axle and main strut is probably caused by the difficulties in modeling flows past cylinders in the sub-critical and critical regime. Compared to the mean pressure, a better grid convergence was noticed for the unsteady pressure PSDs but large under-predictions were seen at some Kulite locations on the main strut and axle. Large grid sensitivities and significant differences between the simulation and the experimental PIV results were observed for the mean velocity fields. The major discrepancies are in the core of the wake right downstream of the landing gear. Nevertheless, the velocity PSDs computed with simulations have reasonable comparison with the experimental results and exhibit grid convergence in the low frequency range at probes inside the wake of the wheels.

With the effects of tripping, the simulation results have smaller grid sensitivities and better comparison with the experimental data at regions near the axle and main strut, as well as the wake region. First of all, the mean pressure coefficients on the strut and axle are closer to the experimental values, with much less grid sensitivities. The pressure PSDs on those gear components are also improved to higher levels and have much closer agreements with the experimental results. The tripping in the experiments triggered transition to turbulence at more upstream boundary layer locations on the main strut and axle, thus the flows around those cylindrical components are similar to flows at higher Reynolds number regime. In general, higher grid resolution is required for good predictions of pressure PSDs, compared to the mean pressure, for probes on the wheels. Large non-local effects on the pressure PSDs from the tripping, the corners and curvatures of the geometry, and the wake, were experienced which indicate that some WMLES grid resolution guidelines [63] for capturing pressure fluctuations generated from flat-plate boundary layers may not be directly applicable to this complex problem. Alternate approaches such as proper orthogonal decomposition (POD) [64, 65] which capture spatio-temporal coherence can be used to identify such non-local effects and facilitate

further targeted grid refinements. The magnitudes and topologies of the mean velocity components in the turbulent wake were found to be more similar to those from the experimental measurements with numerical tripping. The PSDs of the velocity components inside the wake are also improved with higher cut-off frequencies with the tripping.

Considering the far-field noise predictions using the FWH acoustic analogy with solid FWH surface, the computed results have decent grid convergence and agreements with the experimental results up to 4 kHz. Nevertheless, over-predictions in the PSD levels were observed in the higher frequency range with the high-resolution CFD grids and each level of grid-refinement shows a larger over-prediction compared to the microphone data for frequencies greater than 4kHz, most-noticeably for observers located on the sideline plane. The effects of tripping on the far-field noise were observed to be insignificant although the near-field results, especially the mean velocity of the wake, were found to be very sensitive to the numerical tripping. The results obtained using low resolution CFD grid with 2.4 mm finest grid spacing (grid B) has surprisingly good comparison with the experimental results, despite poor predictions of the near-field noise levels, compared to the high resolution cases. This contradiction was also observed in previous literature works and this leads to the questioning of the suitability of solid/impermeable FWH approach for this problem with WMLES. In the future work, the use of the permeable FWH method, which is a more general and correct approach, for the far-field noise predictions will be examined and compared with the solid FWH approach for this problem with WMLESs.

Acknowledgments

This work was partially funded by the Transformational Tools and Technologies (TTT) and the Commercial Supersonic Technology (CST) projects. Computer time has been provided by the NASA Advanced Supercomputing (NAS) facility at NASA Ames Research Center. We gratefully acknowledge Dr. Michael F. Barad, Dr. Jeffrey A. Housman, Dr. Jordan B. Angel, and Dr. Ercan Dumlupinar of NASA Ames Research Center for valuable discussions. We would also like to thank Dr. Eric Manoha from ONERA for providing the geometry and experimental data of the LAGOON benchmark problem.

References

[1] Basner, M., Clark, C., Hansell, A., Hileman, J. I., Janssen, S., Shepherd, K., and Sparrow, V., "Aviation noise impacts: state of the science," *Noise & health*, Vol. 19, No. 87, 2017, p. 41.

[2] Thomas, R. H., Guo, Y., Berton, J., and Fernandez, H., "Aircraft noise reduction technology roadmap toward achieving the nasa 2035 goal," *23rd AIAA/CEAS aeroacoustics conference*, 2017, p. 3193.

[3] Krein, A., and Williams, G., "Flightpath 2050: Europe's vision for aeronautics," *Innovation for Sustainable Aviation in a Global Environment: Proceedings of the Sixth European Aeronautics Days, Madrid*, Vol. 30, 2012.

[4] Zhao, K., Okolo, P., Neri, E., Chen, P., Kennedy, J., and Bennett, G. J., "Noise reduction technologies for aircraft landing gear-A bibliographic review," *Progress in Aerospace Sciences*, Vol. 112, 2020, p. 100589.

[5] Dobrzynski, W., Chow, L., Guion, P., and Shiells, D., "A European study on landing gear airframe noise sources," *6th Aeroacoustics Conference and Exhibit*, 2000, p. 1971.

[6] Li, Y., Smith, M. G., and Zhang, X., "Identification and attenuation of a tonal-noise source on an aircraft's landing gear," *Journal of Aircraft*, Vol. 47, No. 3, 2010, pp. 796–804.

[7] Dobrzynski, W., "Almost 40 years of airframe noise research: what did we achieve?" *Journal of aircraft*, Vol. 47, No. 2, 2010, pp. 353–367.

[8] Manoha, E., Bulté, J., and Caruelle, B., "LAGOON: an experimental database for the validation of CFD/CAA methods for landing gear noise prediction," *14th AIAA/CEAS aeroacoustics conference (29th AIAA aeroacoustics conference)*, 2008, p. 2816.

[9] Manoha, E., Bulté, J., Ciobaca, V., and Caruelle, B., "LAGOON: further analysis of aerodynamic experiments and early aeroacoustics results," *15th AIAA/CEAS aeroacoustics conference (30th AIAA aeroacoustics conference)*, 2009, p. 3277.

[10] Sanders, L., Manoha, E., Ben Khelil, S., and Francois, C., "LAGOON: CFD/CAA coupling for landing gear noise and comparison with experimental database," *17th AIAA/CEAS Aeroacoustics Conference (32nd AIAA Aeroacoustics Conference)*, 2011, p. 2822.

[11] Sanders, L., Manoha, E., Ben Khelil, S., and Francois, C., "LAGOON: New Mach Landing Gear Noise Computation and further analysis of the CAA process," *18th AIAA/CEAS aeroacoustics conference (33rd AIAA aeroacoustics conference)*, 2012, p. 2281.

[12] Sanders, L., Manoha, E., Ben Khelil, S., and François, C., "CFD/CAA coupling on the LAGOON# 2 landing gear using a structured multi-block solver with the Chimera technique," *19th AIAA/CEAS aeroacoustics conference*, 2013, p. 2257.

[13] Giret, J.-C., Sengissen, A., Moreau, S., and Jouhaud, J.-C., "Prediction of LAGOON landing-gear noise using an unstructured LES Solver," *19th AIAA/CEAS aeroacoustics conference*, 2013, p. 2113.

[14] Liu, W., Kim, J. W., Zhang, X., Angland, D., and Caruelle, B., "Landing-gear noise prediction using high-order finite difference schemes," *Journal of Sound and Vibration*, Vol. 332, No. 14, 2013, pp. 3517–3534.

[15] Casalino, D., Ribeiro, A. F., Fares, E., and Nölting, S., "Lattice–Boltzmann aeroacoustic analysis of the LAGOON landing-gear configuration," *AIAA journal*, Vol. 52, No. 6, 2014, pp. 1232–1248.

[16] de la Puente, F., Sanders, L., and Vuillot, F., "On LAGOON nose landing gear CFD/CAA computation over unstructured mesh using a ZDES approach," *20th AIAA/CEAS aeroacoustics conference*, 2014, p. 2763.

[17] Manoha, E., and Caruelle, B., "Summary of the LAGOON solutions from the Benchmark problems for Airframe Noise Computations-III Workshop," *21st AIAA/CEAS aeroacoustics conference*, 2015, p. 2846.

[18] Sengissen, A., Giret, J.-C., Coreixas, C., and Boussuge, J.-F., "Simulations of LAGOON landing-gear noise using lattice Boltzmann solver," *21st AIAA/CEAS aeroacoustics conference*, 2015, p. 2993.

[19] Larsson, J., Kawai, S., Bodart, J., and Bermejo-Moreno, I., "Large eddy simulation with modeled wall-stress: recent progress and future directions," *Mechanical Engineering Reviews*, Vol. 3, No. 1, 2016, pp. 15–00418.

[20] Kocheemoolayil, J. G., and Lele, S. K., "Large Eddy Simulation of Airfoil Self-Noise at High Reynolds Number," *22nd AIAA/CEAS Aeroacoustics Conference*, 2016, p. 2919.

[21] Zhang, Y., Chen, H., Wang, K., and Wang, M., "Aeroacoustic prediction of a multi-element airfoil using wall-modeled large-eddy simulation," *AIAA Journal*, Vol. 55, No. 12, 2017, pp. 4219–4233.

[22] Kiris, C. C., Housman, J. A., Barad, M. F., Brehm, C., Sozer, E., and Moini-Yekta, S., "Computational framework for launch, ascent, and vehicle aerodynamics (LAVA)," *Aerospace Science and Technology*, Vol. 55, 2016, pp. 189–219.

[23] Ghate, A. S., Housman, J. A., Stich, G.-D., Kenway, G., and Kiris, C. C., "Scale resolving simulations of the NASA Juncture Flow Model using the LAVA solver," *AIAA Aviation 2020 Forum*, 2020, p. 2735.

[24] Ghate, A. S., Kenway, G. K., Stich, G.-D., Browne, O. M., Housman, J. A., and Kiris, C. C., "Transonic lift and drag predictions using Wall-Modelled Large Eddy Simulations," *AIAA Scitech 2021 Forum*, 2021, p. 1439.

[25] Stich, G.-D., Housman, J. A., Ghate, A. S., and Kiris, C. C., "Jet Noise Prediction with Large-Eddy Simulation for Chevron Nozzle Flows," *AIAA Scitech 2021 Forum*, 2021, p. 1185.

[26] Stich, G.-D., Ghate, A. S., Housman, J. A., and Kiris, C. C., "Wall Modeled Large Eddy Simulations for NASA's jet noise consensus database of single-stream, round, convergent jets." *AIAA SCITECH 2022 Forum*, 2022, p. 0684.

[27] Stich, G.-D., Ghate, A. S., Housman, J. A., and Kiris, C. C., "Wall-Modeled Large-Eddy Simulations of Jet Noise in Flight Conditions," *28th AIAA/CEAS Aeroacoustics Conference*, 2022.

[28] Farassat, F., and Succi, G. P., "The prediction of helicopter rotor discrete frequency noise," *In: American Helicopter Society*, 1982, pp. 497–507.

[29] Barad, M. F., Kocheemoolayil, J. G., and Kiris, C. C., "Lattice Boltzmann and Navier-stokes cartesian cfd approaches for airframe noise predictions," *23rd AIAA Computational fluid dynamics conference*, 2017, p. 4404.

[30] Manoha, E., and Caruelle, B., "LAGOON Simplified (2-Wheel) Nose Landing Gear Configuration# 1 Experimental Database," Tech. rep., Technical Report, 2011.

[31] Nonomura, T., and Fujii, K., "Robust explicit formulation of weighted compact nonlinear scheme," *Computers & Fluids*, Vol. 85, 2013, pp. 8–18.

[32] Wong, M. L., and Lele, S. K., "High-order localized dissipation weighted compact nonlinear scheme for shock-and interface-capturing in compressible flows," *Journal of Computational Physics*, Vol. 339, 2017, pp. 179–209.

[33] Jiang, G.-S., and Shu, C.-W., "Efficient implementation of weighted ENO schemes," *Journal of computational physics*, Vol. 126, No. 1, 1996, pp. 202–228.

[34] Deng, X., and Zhang, H., "Developing high-order weighted compact nonlinear schemes," *Journal of Computational Physics*, Vol. 165, No. 1, 2000, pp. 22–44.

[35] Nonomura, T., Iizuka, N., and Fujii, K., "Increasing order of accuracy of weighted compact nonlinear scheme," *AIAA Paper*, Vol. 893, 2007.

[36] Zhang, S., Jiang, S., and Shu, C.-W., "Development of nonlinear weighted compact schemes with increasingly higher order accuracy," *Journal of Computational Physics*, Vol. 227, No. 15, 2008, pp. 7294–7321.

[37] Subramaniam, A., Wong, M. L., and Lele, S. K., "A high-order weighted compact high resolution scheme with boundary closures for compressible turbulent flows with shocks," *Journal of Computational Physics*, Vol. 397, 2019, p. 108822.

[38] Wong, M. L., Angel, J. B., Barad, M. F., and Kiris, C. C., "A positivity-preserving high-order weighted compact nonlinear scheme for compressible gas-liquid flows," *Journal of Computational Physics*, Vol. 444, 2021, p. 110569.

[39] Toro, E. F., Spruce, M., and Speares, W., "Restoration of the contact surface in the HLL-Riemann solver," *Shock waves*, Vol. 4, No. 1, 1994, pp. 25–34.

[40] Einfeldt, B., "On Godunov-type methods for gas dynamics," *SIAM Journal on Numerical Analysis*, Vol. 25, No. 2, 1988, pp. 294–318.

[41] Einfeldt, B., Munz, C.-D., Roe, P. L., and Sjögreen, B., "On Godunov-type methods near low densities," *Journal of Computational Physics*, Vol. 92, No. 2, 1991, pp. 273–295.

[42] Batten, P., Clarke, N., Lambert, C., and Causon, D., "On the choice of wavespeeds for the HLLC Riemann solver," *SIAM Journal on Scientific Computing*, Vol. 18, No. 6, 1997, pp. 1553–1570.

[43] Shu, C.-W., and Osher, S., "Efficient implementation of essentially non-oscillatory shock-capturing schemes, II," *Journal of Computational Physics*, Vol. 83, No. 1, 1989, pp. 32–78.

[44] Piomelli, U., and Balaras, E., "Wall-layer models for large-eddy simulations," *Annual review of fluid mechanics*, Vol. 34, No. 1, 2002, pp. 349–374.

[45] Piomelli, U., "Wall-layer models for large-eddy simulations," *Progress in aerospace sciences*, Vol. 44, No. 6, 2008, pp. 437–446.

[46] Bose, S. T., and Park, G. I., "Wall-modeled large-eddy simulation for complex turbulent flows," *Annual review of fluid mechanics*, Vol. 50, 2018, pp. 535–561.

[47] Vreman, A., "An eddy-viscosity subgrid-scale model for turbulent shear flow: Algebraic theory and applications," *Physics of fluids*, Vol. 16, No. 10, 2004, pp. 3670–3681.

[48] Tseng, Y.-H., and Ferziger, J. H., "A ghost-cell immersed boundary method for flow in complex geometry," *Journal of computational physics*, Vol. 192, No. 2, 2003, pp. 593–623.

[49] Seifert, A., and Pack, L. G., "Active flow separation control on wall-mounted hump at high Reynolds numbers," *AIAA journal*, Vol. 40, No. 7, 2002, pp. 1363–1372.

[50] Kiris, C. C., Stich, D., Housman, J. A., Kocheemoolayil, J. G., Barad, M. F., and Cadieux, F., "Application of Lattice Boltzmann and Navier-Stokes methods to NASA's wall mounted hump," *2018 Fluid Dynamics Conference*, 2018, p. 3855.

[51] Addy, H. E., *Ice accretions and icing effects for modern airfoils*, National Aeronautics Administration, Glenn Research Center, 2000.

[52] Ghate, A. S., Kenway, G. K. W., Stich, G.-D., Maldonado, D., and Kiris, C. C., "A Wall-Modeled LES Perspective for the High Lift Common Research Model Using LAVA," *AIAA Aviation Paper to appear*, 2022.

[53] Neuhart, D., Khorrami, M., and Choudhari, M., "Aerodynamics of a Gulfstream G550 nose landing gear model," *15th AIAA/CEAS Aeroacoustics Conference (30th AIAA Aeroacoustics Conference)*, 2009, p. 3152.

[54] Rodríguez, I., Lehmkuhl, O., Chiva, J., Borrell, R., and Oliva, A., "On the flow past a circular cylinder from critical to super-critical Reynolds numbers: Wake topology and vortex shedding," *International Journal of Heat and Fluid Flow*, Vol. 55, 2015, pp. 91–103.

[55] Ricciardi, T. R., Wolf, W. R., and Speth, R., "Acoustic prediction of LAGOON landing gear: cavity noise and coherent structures," *AIAA Journal*, Vol. 56, No. 11, 2018, pp. 4379–4399.

[56] Williams, J. F., and Hawkings, D. L., "Sound generation by turbulence and surfaces in arbitrary motion," *Philosophical Transactions for the Royal Society of London. Series A, Mathematical and Physical Sciences*, 1969, pp. 321–342.

[57] Di Francescantonio, P., "A new boundary integral formulation for the prediction of sound radiation," *Journal of Sound and Vibration*, Vol. 202, No. 4, 1997, pp. 491–509.

[58] Brentner, K. S., "Prediction of helicopter rotor discrete frequency noise: A computer program incorporating realistic blade motions and advanced acoustic formulation," Tech. rep., 1986.

[59] Garrick, I., and Watkins, C. E., "A theoretical study of the effect of forward speed on the free-space sound-pressure field around propellers," Tech. rep., 1953.

[60] Lockard, D., "A comparison of Ffowcs Williams-Hawkings solvers for airframe noise applications," *8th AIAA/CEAS Aeroacoustics Conference & Exhibit*, 2002, p. 2580.

[61] Bres, G., Pérot, F., and Freed, D., "A Ffowcs Williams-Hawkings solver for Lattice-Boltzmann based computational aeroacoustics," *16th AIAA/CEAS aeroacoustics conference*, 2010, p. 3711.

[62] Spalart, P. R., Belyaev, K. V., Shur, M. L., Kh Strelets, M., and Travin, A. K., "On the differences in noise predictions based on solid and permeable surface Ffowcs Williams–Hawkings integral solutions," *International Journal of Aeroacoustics*, Vol. 18, No. 6-7, 2019, pp. 621–646.

[63] Park, G. I., and Moin, P., "Space-time characteristics of wall-pressure and wall shear-stress fluctuations in wall-modeled large eddy simulation," *Physical review fluids*, Vol. 1, No. 2, 2016, p. 024404.

[64] Towne, A., Schmidt, O. T., and Colonius, T., "Spectral proper orthogonal decomposition and its relationship to dynamic mode decomposition and resolvent analysis," *Journal of Fluid Mechanics*, Vol. 847, 2018, pp. 821–867.

[65] Ghate, A. S., Ghaisas, N., Lele, S. K., and Towne, A., "Interaction of small scale homogenenous isotropic turbulence with an actuator disk," *2018 Wind Energy Symposium*, 2018, p. 0753.